Nuclear Science and Engineering

ISSN: 0029-5639 (Print) 1943-748X (Online) Journal homepage: www.tandfonline.com/journals/unse20

# A Reactor Transient Benchmark for Molten Salt Reactor Experiment Pump Transient Tests

**Mohamed Elhareef, Youssef Abouhussien, Zeyun Wu, Massimiliano Fratoni, Eva Davidson, Tingzhou Fei & Kurt Harris**

**To cite this article:** Mohamed Elhareef, Youssef Abouhussien, Zeyun Wu, Massimiliano Fratoni, Eva Davidson, Tingzhou Fei & Kurt Harris (05 May 2025): A Reactor Transient Benchmark for Molten Salt Reactor Experiment Pump Transient Tests, Nuclear Science and Engineering, DOI: 10.1080/00295639.2025.2475650

**To link to this article:** https://doi.org/10.1080/00295639.2025.2475650

NUCLEAR SCIENCE AND ENGINEERING

DOI: https://doi.org/10.1080/00295639.2025.2475650



# A Reactor Transient Benchmark for Molten Salt Reactor Experiment Pump Transient Tests

Mohamed Elhareef,[a] Youssef Abouhussien,[a] Zeyun Wu,[a]* Massimiliano Fratoni,[b] Eva Davidson,[c] Tingzhou Fei,[d] and Kurt Harris[e]

[a]*Virginia Commonwealth University, Department of Mechanical and Nuclear Engineering, Richmond, Virginia 23284*
[b]*University of California, Department of Nuclear Engineering, Berkeley, California 94710*
[c]*Oak Ridge National Laboratory, Oak Ridge, Tennessee 37831*
[d]*Argonne National Laboratory, Lemont, Illinois 60439*
[e]*Flibe Energy, Inc, Huntsville, Alabama 35806*

Received August 22, 2024
Accepted for Publication February 24, 2025

**Abstract** — *The molten salt reactor is one candidate among the Generation IV nuclear reactor designs, with its deployment relying on advanced computational tools to capture the unique behavior of the circulating fuel system. The Molten Salt Reactor Experiment (MSRE) provides valuable experimental data for validating these computational tools. This work develops a reactor transient benchmark based on the MSRE pump transient tests.*

*Two computational models are evaluated in the benchmark: a simplified one-dimensional (1D) system-level model and a more detailed R-Z axisymmetric model using the porous medium approximation. The models are used to evaluate the impact of spatial resolution on predicted reactivity responses during the transient. Several impactful factors are examined during the benchmark evaluation, including the neutron diffusion multigroup energy structure, delayed neutron precursor (DNP) diffusion, DNP group structure, bypass flow, and transient flow rates.*

*The reactivity predictions using the computational models are compared to the experimental data. The mean errors in the predicted reactivity responses ranged from 11 to 21 pcm (1 pcm = $10^{-5}$) for the pump startup transient and 5 to 13 pcm for the pump coastdown transient. These results indicate that the 1D model can provide adequate accuracy on MSRE pump transients with limitations in predicting the rate of reactivity at the early stage of the transient, while the higher-order model improves this capability by incorporating the influence of radial salt flow distribution and bypass flow on transient reactivity.4*

**Keywords** — *Molten salt reactor, Molten Salt Reactor Experiment, reactor benchmark, pump transient, multiphysics modeling.*

**Note** — *Some figures may be in color only in the electronic version.*

## I. INTRODUCTION

The molten salt reactor (MSR) is one of the six high-potential Generation IV nuclear reactor technologies.[1] In these designs, the fissile isotopes are dissolved in a molten salt mixture and circulated in the primary loop. The safety advantages of this class of reactors include low operating pressures, elimination of fuel meltdown concerns, the possibility of fuel drain into a passive configuration, and both irradiation and thermal stability of the fluoride salts.[2]

*E-mail: zwu@vcu.edu

The nonsafety advantages include compact design, a small facility footprint, high potential thermal-to-electric conversion efficiency, continued online refueling and fission product removal, minimal fuel fabrication and certification costs, and fuel flexibility ranging from using enriched uranium in an open fuel cycle, thorium in a closed breeder fuel cycle, or even unwanted transuranic elements from existing used nuclear fuel or weapons inventories. These advantages position MSR technology as a highly attractive option for the industry, driving increased interest and investment in research, development, and demonstration activities.[3]

The adoption of circulating liquid fuels results in some intriguing physical phenomena, such as the fact that the delayed neutron source distribution is not proportional to the in-core power distribution, as in solid-fueled reactors. Instead, the delayed neutron source varies with the fuel flow due to the distribution of the delayed neutron precursors (DNP) throughout the fuel circulation loop as a function of the flow field. Similarly, the fission product circulation and removal system affect the decay heat distribution and neutron balance.

Another unique aspect of liquid fuels is that the heat is generated directly in the coolant, creating a strong coupling between the neutronics and thermal-hydraulic behaviors. These phenomena are challenging for the well-established computational methods that are optimized for stationary fuel reactors. Another major challenge facing the development of the MSR is the lack of evaluated experimental data that can be used for validating computational methods.

The Molten Salt Reactor Experiment (MSRE) was an 8-MW(thermal), thermal spectrum, circulating fuel reactor that aimed to demonstrate the safety and practicality of MSRs, as well as to provide long-term irradiation tests of fuel, nickel-based alloy INOR-8, and graphite under actual service conditions.[4] This experiment is currently considered the only reliable source for experimental data for MSRs. The construction of the MSRE was completed in 1964, and it reached criticality on June 1, 1965. After completing 13 000 equivalent full power hours of operation using $^{235}$U, phase one of operation was successfully concluded.[5] The second phase started in August 1968 when 91% enriched $^{233}$U was added, making the MSRE the first reactor to operate using this fissile isotope. The MSRE was put in shutdown conditions in January 1970.[6] The MSRE is extensively used to validate computational tools for circulating fuel reactors.[7–11]

During the operation of the MSRE, several static, dynamic, and transient experiments were conducted to address the reactor physics features of the circulating fuel system. Over the years, researchers have used these tests to validate various methods and computational tools for MSRs. Křepel et al.[12] used the MSRE benchmark data defined by the Molten Salt Reactor Technology (MOST) project[9] for validating the code DYN3D-MSR. Jaradat et al.[13] developed transient capabilities for MSRs in the neutron transport code PROTEUS-NODAL and validated the code against the data from the MSRE pump transients and natural circulation tests. The steady-state data of the MSRE was used to validate Moltres, a MOOSE-based model for MSRs.[14] The MSRE data have also been used to validate the multiphysics coupling between neutronics and thermal-fluidic codes.[15,16]

The results of all these activities have resulted in unresolved discrepancies between the experimental data and the simulation results. One reason for this continuing issue is the lack of a systematic evaluation of the experimental data, system specifications, and test procedures, which we hope to fix. The aim of this work is to identify the sources of uncertainty in the experimental data for the MSRE pump transient tests and to evaluate the impact of various modeling choices on the simulation results.

With this motivation, this work focused on the approaches to developing an evaluated reactor transient benchmark derived from the MSRE pump transient tests for the International Reactor Physics Experiment Evaluation Project (IRPhE) Handbook.[17] The IRPhE Handbook serves as a collection of evaluated reactor physics benchmarks that have been derived from various experiments. The aim of this Handbook is to provide benchmark specifications for reactor designers and safety analysts and to validate calculational techniques.[18] A static benchmark for MSRs based on the MSRE has been included[19] in the IRPhE Handbook starting with the 2019 edition.

This work aims to add a transient benchmark to the existing static benchmark. To achieve this objective, a thorough review of the test procedure and measurement system was performed. The sources of uncertainty were identified and propagated to the reactivity response. Finally, two distinctive benchmark models were provided, and isolated effect studies were performed to understand the impact of the various model simplifications.

In this work, the uncertainty in the experimental data was evaluated based on the available information about the measurement system. A sampling approach was used to provide an estimation of the uncertainty in the experimental data. Two computational models at different orders were developed and employed to evaluate the impact of various modeling choices and geometrical features of the MSRE. The low-order model used a one-dimensional (1D)

geometrical representation of the MSRE primary loop and a fully coupled neutronics/fluid flow model. A fully coupled scheme means that all equations were solved simultaneously by assembling all equations in a single global matrix system.

The high-order model used a R-Z two-dimensional (2D) geometrical representation of the MSRE and an iterative multiphysics coupling scheme to achieve the numerically converged solutions. An iterative approach was used for the R-Z model due to the large number of degrees of freedom. The parameters investigated in this work included the multigroup energy structure, the diffusion coefficient of DNP, the DNP group structure, the bypass flow, and the uncertainty in the transient flow rate driving the reactivity transient.

The remainder of this paper is organized as follows. Section I provides a detailed description of the MSRE system, the pump transient tests, and the evaluation of the uncertainty in experimental data. Section III provides theorical descriptions of the two mathematical models used in this work. Sections IV and V discuss the results of the MSRE transient benchmark based on the low-order model and the high-order model, respectively. Finally, Sec. VI offers the main conclusion remarks drawn from this work.

## II. MSRE PUMP TRANSIENT TESTS

### II.A. System Specifications

The MSRE consisted of two salt circulation loops. The fuel circulation loop (i.e., primary loop) consisted of the reactor vessel, the primary pump, the shell side of the heat exchanger (HX), and the connecting piping. The coolant circulating loop consisted of the tube side of the HX, the secondary pump, the radiator, and the connecting piping.

The fuel carrying salt was FLiBe, with a composition of LiF-$BeF_2$-$ZrF_4$-$UF_4$ (65.0%-29.17%-5.0%-0.83%) at initial critical loading.[20] The $^{235}U$ enrichment was 31.35 wt% and the $^{7}Li$ enrichment was 99.995 wt%. The coolant salt had the composition of LiF-$BeF_2$ (66%-34%). The moderator was a grade CGB[21] graphite matrix that was formed into vertical bars (stringers) arrayed to form a core structure that provided salt flow channels.

Reactivity control was provided through three flexible solid control rods of gadolinium oxide positioned where three graphite stringers were removed and located equidistant from the center of the graphite matrix.[20] A fourth stringer was left out for the sample basket. All structural materials were made of nickel-based alloy INOR-8 (Hastelloy N). A detailed description of the MSRE materials and neutronics considerations can be found in Ref. [19]. The thermophysical properties of the fuel salt are listed in Table I.

The MSRE reactor vessel had a height of 8 ft (2.44 m), an inner diameter of 58 in. (1.47 m), and a thickness of 9/16 in. (1.43 cm) at the cylindrical portion and 1 in. (2.54) at the flow distributer, upper head, and lower head regions. The lower and upper heads of the vessel were torispherical domes with an inner diameter of 58 in. (1.47 m). The aspect ratio of the vessel heads (i.e., diameter-to-height ratio) was about 4.28.

The fuel salt entered the vessel through a 5-in (12.7-cm) schedule 40 inlet nozzle. The inlet nozzle was tangent to the flow distributor, which was a half-circular torus with an inner diameter of 4 in. (10.16 cm). The flow was distributed evenly around the circumference of the vessel and entered the vessel through 84 holes with a 3/4-in. (1.91-cm) diameter arranged in three rows and with a 30-deg tangent on the outer surface of the vessel to promote spiral flow around the vessel. The salt then flowed spirally downward in the annulus, which was formed in the 1-in. (2.54-cm) gap between the vessel wall and the core can. The core can was a 1/4-in. (0.64-cm) cylindrical shell with a 68-in. (1.73-m) height and a 55.5-in. (1.41-m) inner diameter.

The salt exited the bottom of the annulus and flowed radially in the lower head guided by 48 radial swirl-straightening vanes of a 11-in. (27.94-cm) length toward the head center. The fuel then flowed upward to the graphite core. The graphite matrix was supported by a lattice of graphite blocks arranged horizontally in two layers at right angles to each other, which in turn was

TABLE I

Thermophysical Properties of the MSRE Fuel Salt[22]

| Property | Fuel Salt | Uncertainty |
|---|---|---|
| Density, $\rho$(kg/m$^3$) | $2575-0.513T(^\circ C)$ | ±1% |
| Heat capacity, $c_p$ (J/kg·K) | 2386.47 | ±3% |
| Thermal conductivity, $k$(W/m·K) | 1.0 | ±10% |
| Dynamic viscosity, $\mu$ (Pa·s) | $11.6 \times 10^{-5} e^{\frac{3755}{T(K)}}$ | ±7% |

supported by a grid of INOR-8 plates. The graphite core was formed by 513 2 × 2-in. (5.08 × 5.08 cm) and 104 fractional-sized vertical, close-packed bars.

Flow channels were formed by grooves on the four faces of each stringer. The flow channel was a stadium-shaped channel with the straight section 0.8 in. (2.032 cm) long and 0.4 in. (1.02 cm) wide, and the round section was a half-circle with a radius of 0.2 in. (0.51 cm). There were 1108 full-sized flow passages, and the flow channels totaled to the equivalent of 1140 full-sized passages. The top horizontal faces of the stringers were tapered to prevent salt accumulation after drainage. The graphite core had a height of about 63 in. (1.6 m) and a diameter of 55.25 in. (1.4 m), leaving a 1/4-in. (0.64-cm) gap between the matrix and the core can. The graphite volume in the core was about 69 $ft^3$ (1.95 $m^3$).

The fuel salt left the graphite matrix and flowed to the upper head, which directed the flow to the outlet nozzle. To promote flow circulation near the walls of the upper head, the fuel flow bypassed directly from the anulus to the upper head through 18 slots, 0.2 × 0.2 in. (5.08 × 5.08 cm) cut in the core can flange. At nominal flow rate (1200 gpm or 0.0757 $m^3/s$), this bypass flow was 24 gpm. There was additional flow (3 to 22 gpm) passing through the annular clearances at the core can support ring.[20]

The upper head had a 10-in. (25.4-cm) nozzle opening that diverted the fuel salt into the 5-in. (12.7-cm) horizontal outlet nozzle. The 10-in. nozzle was provided with a strainer to prevent large chips of graphite from circulating with the fuel salt. A detailed computer-aided design (CAD) model for the MSRE reactor vessel was developed and made publicly available by a team from Copenhagen Atomics.[23] A cut-away drawing of the MSRE reactor vessel is shown in Fig. 1.

A schematic representation on the fuel salt circulation loop is given in Fig. 2, with the numbers of the figure defined in Table II. After leaving the reactor vessel outlet nozzle, the fuel salt flowed through a pipeline (line 100) to the pump suction nozzle. In the MSRE, each pipeline was given a number in the flowcharts. The position of each pipeline relevant to the fuel circulation loop is described in Table II. Line 100 extends 6 ft (1.83 m) in the horizontal direction, with a cross section of 5-in. (12.7-cm) schedule 40, followed with a vertical transition with a length of 32 in. (81.28 cm) and a diameter varying from 5 in. (12.7 cm) to 8 in. (20.32 cm) to match the pump inlet.

The primary pump was a sump-type centrifugal pump that rotated at 1160 rpm to deliver 1200 gpm at discharge head of 48.5 ft (14.78 m). The pump bowl was 36 in. (91.44 cm) in diameter. The pump intake nozzle was 8 in (20.32 cm), and the discharge nozzle was 5 in. (12.7 cm). The pump impeller diameter was 11.5 in. (29.21 cm), and the pump motor was 75 hp. The normal operating volume of the pump was 4.1 $ft^3$ (0.116 $m^3$). A cover gas was provided by helium at a circulation rate of 200 $ft^3$/day, which also served to sweep highly radioactive gases.

The fuel salt was then discharged to the shell side of the HX through line 101. Line 101 was a 5-in. (12.7-cm) schedule 40 with a length of 3.5 ft (1.067 m). The HX was designed for a heat load of 10 MW following the configuration of conventional 25% cut, baffled shell-and-tube units. The HX was installed horizontally with a 3-deg downward pitch. The shell side was 8 ft and 3 in. (2.51 m) long with a 16-in. (40.64-cm) diameter. The tube side consisted of 159 U-tubes with average length of 14 ft (4.27 m) and a 1/2-in. (1.27-cm) outer diameter with 0.042-in.-thick (0.1067-cm) walls.

The effective heat transfer area was about 254 $ft^2$ (23.6 $m^2$). The fuel salt was recirculated to the reactor vessel through line 102, which extended for 5.5 ft (1.68 m). The fuel salt volumes in the primary loop and residence time at the design flow rate (1200 gpm) are listed in Table II.

The coolant salt (secondary salt) left the HX and flowed to the tube side of the radiator where it was cooled by air. The radiator consisted of 120 S-shaped tubes, with each tube 30 ft (9.14 m) in length with a 3/4-in. (1.91-cm) outer diameter and a 0.072-in. (0.183-cm) wall thickness. The tubes were arranged in a staggered configuration with 12 tubes in height and 10 tubes in depth. The effective heat transfer area was 706 $ft^2$ (65.59 $m^2$).

The coolant salt then flowed to the suction line of the secondary pump. The secondary pump was almost identical to the primary pump. The secondary pump was designed to deliver 850 gpm (0.0536 $m^3/s$) against a head of 78 ft (23.77 m) when driven at 1750 rpm by a 75-hp motor. The pump intake nozzle was 6 in. (15.24 cm), and the discharge nozzle was 5 in. (12.7 cm). The impeller diameter of the pump was 10.33 in. (26.24 cm). The coolant salt was then recirculated to the HX. The salt volume in the secondary loop was 45.83 $ft^3$ (1.298 $m^3$).

The air was provided by two blowers that had a combined capacity of 200 000 cfm (94.39 $m^3/s$) at a discharge head of 9 in (22.86 cm) of water. The inlet air temperature was 100°F, and the outlet air temperature was 300°F under designed conditions. The radiator was equipped with two doors on the upstream and downstream faces that could move vertically to provide a control on the heat load. Each door was 8 ft (2.44 m)

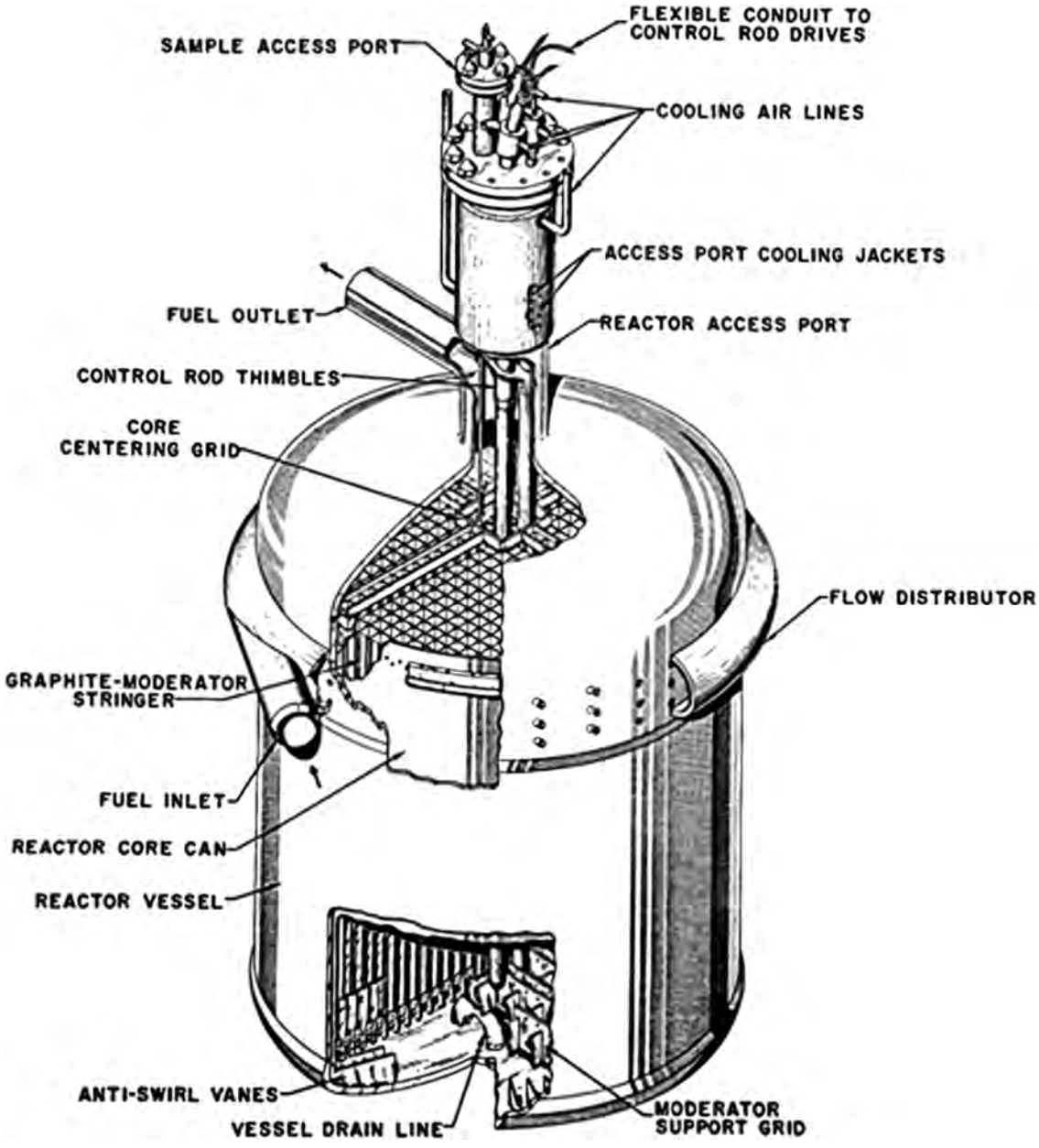


Fig. 1. MSRE reactor vessel (originally Fig. 2.2 in Ref. [20]).

in height and 11 ft (3.35 m) wide and could move at a rate of 10 ft/min (5.08 cm/s).

## II.B. Pump Transient Tests

The MSRE pump transient test was a set of two transients that were conducted at zero power (i.e., isothermal at 1200°F). At this condition, the mass flow rate in the primary loop was 169.746 kg/s. The aims of the pump transient tests were to (1) obtain the fuel pump and coolant pump startup and coastdown characteristics, (2) infer the fuel salt flow rate characteristics during coastdown, and (3) determine the transient effects of fuel flow rate changes on reactivity.[25] The pump transient tests were conducted during the initial phase of MSRE operation with the $^{235}$U fuels. The tests were conducted by interrupting the fuel salt flow rate and measuring the position of the control rod, which was automatically driven to keep the core power at a fixed level.

The regulating control rod was driven by a flux servo controller unit that attempted to maintain the

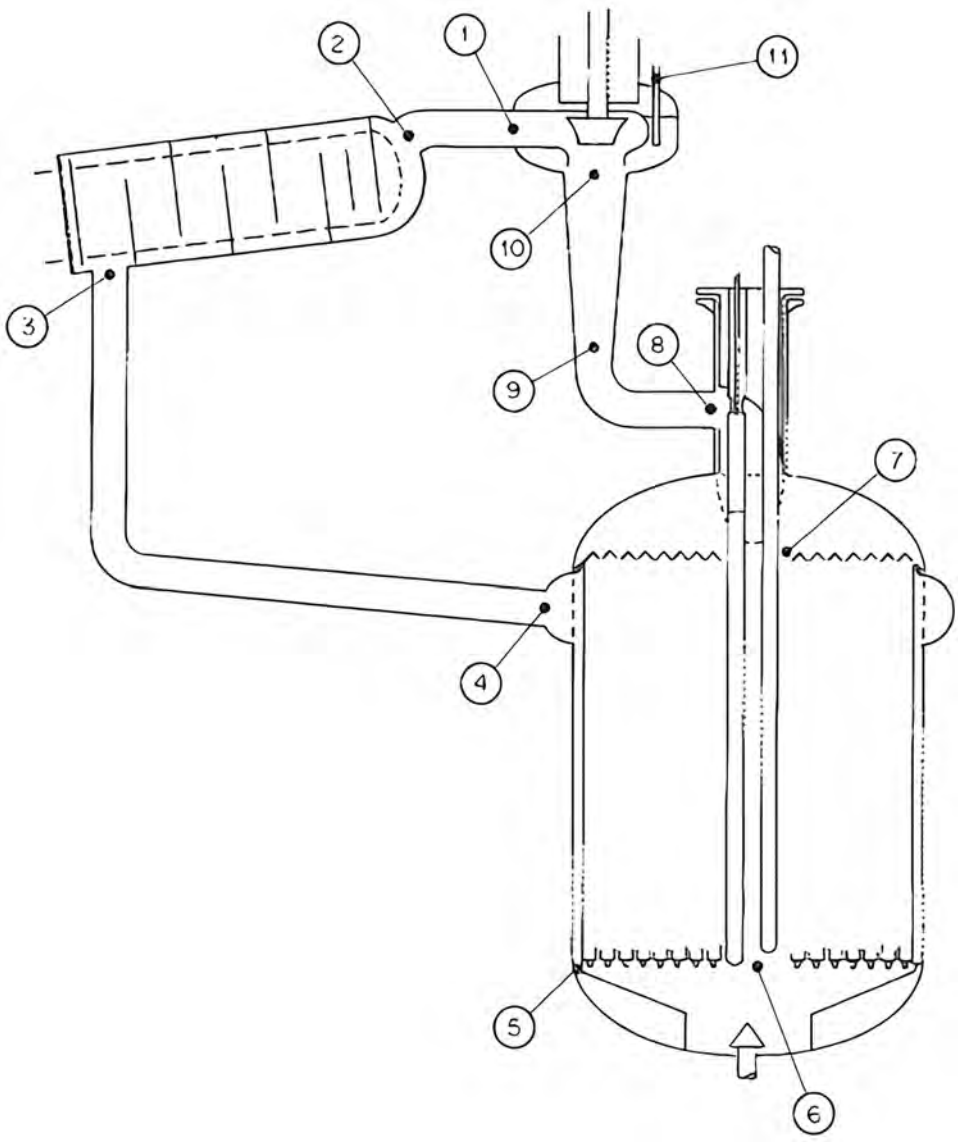


Fig. 2. MSRE fuel circulation loop (originally Fig. 2.2 in Ref. [24]).

flux signal constant. At the test conditions, the reactivity perturbations were entirely attributed to the perturbations in the DNP concentration due to the flow transient.[26] With flow rate changes, the axial and radial distribution of DNP inside the core changed. These changes in the delayed neutron source affected the core criticality and external reactivity (i.e., control rod) was required to compensate for the deviation from criticality.

### *II.B.1. Test Procedures and Measured Data*

The pump startup transient started from the steady-state stationary salt configuration. During the pump startup test, the speeds of both the fuel pump and the coolant pump were increased simultaneously from zero to the rated speed to induce the flow transient. The reactivity effects of the flow transient were measured by recording the control rod position as a function of time, which was controlled by the flux-servo controller unit to maintain criticality. The servo controller movement was controlled by three signals: (1) the measured flux, (2) the flux demand (i.e., desired power level), and (3) the rod speed signal.[27]

Following the startup test, starting from the steady-state flowing condition, the motor of each pump was turned off to initiate the pump coastdown transient. The reactivity effects of this flow transient were measured in a similar manner to the startup test. The control rod

TABLE II

Geometrical Parameters of the MSRE Fuel Circulation Loop[20]

| Component | Position (see Fig. 2) | Volume ($m^3$) | Residence time (s) |
|---|---|---|---|
| Core | 6 and 7 | 0.7080 | 9.3 |
| Upper plenum | 7 and 8 | 0.2973 | 3.9 |
| Line 100 (vessel to pump) | 8 and 10 | 0.0595 | 0.8 |
| Pump — Mainstream | 10 and 1 | 0.0255 | 0.3 |
| Pump — Outside mainstream | | 0.0906 | – |
| Line 101 (pump to HX) | 1 and 2 | 0.0227 | 0.3 |
| HX | 2 and 3 | 0.1727 | 2.3 |
| Line 102 (HX to vessel) | 3 and 4 | 0.0623 | 0.8 |
| Distributor + downcomer | 4 and 5 | 0.2747 | 3.6 |
| Lower plenum | 5 and 6 | 0.2832 | 3.8 |
| Total | | 1.9963 | 25.2 |

response to the pump transient tests and the integral worth curves of the regulating control rod are shown in Fig. 3; the final loading curve was used in this study, as the pump transient test was conducted after the final fuel loading. During the pump transient tests, both the fuel pump speed and coolant pump speed were recorded along with the time, but only the flow rate in the coolant salt loop (i.e., the secondary loop) was recorded.[28]

The transient flow rate in the primary loop is considered missing data. As the initiating event of the reactivity transient, it is important to accurately estimate the transient flow rate in the primary loop. This was done in our previous work[29] by solving the conservation equations of the fluid momentum and the pump angular momentum given the measured pump speed. The detailed procedure for regenerating the missing flow rate is discussed in Ref. [29]. The regenerated normalized primary flow rate during the pump transient tests, along with the estimated uncertainty, are given in Table III. Note that the reported flow rate values were normalized to the nominal flow rate (1200 gpm).

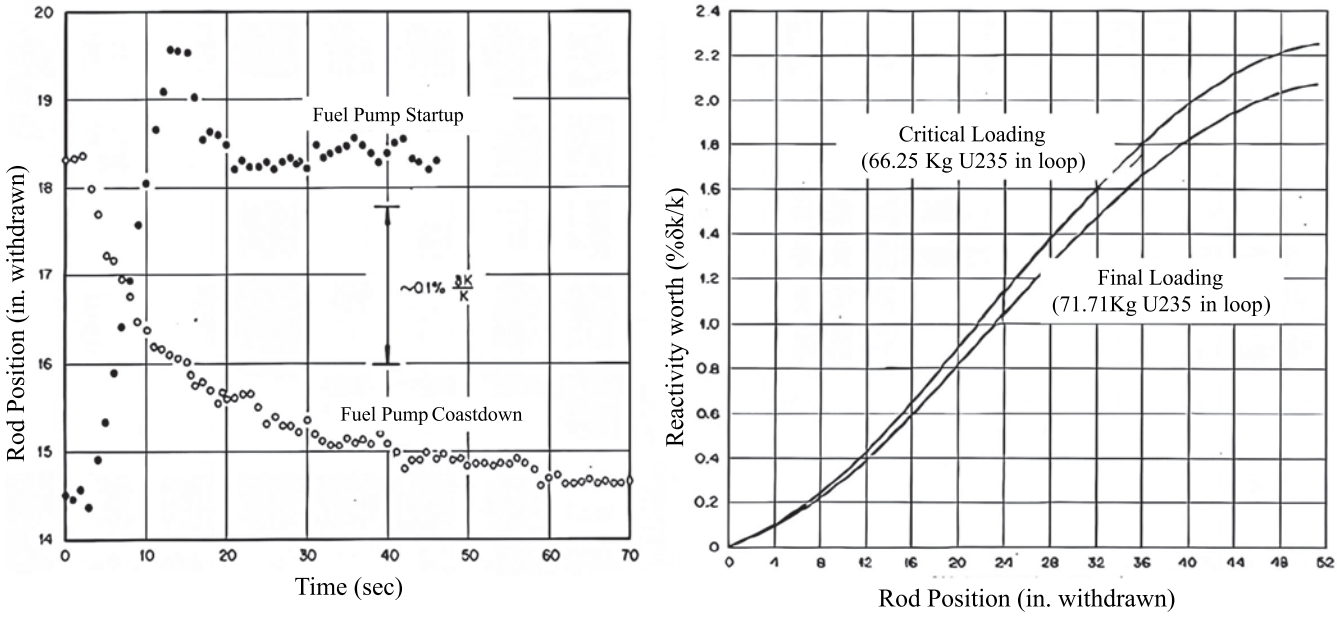


Fig. 3. (left) Experimental measurements for control rod response to fuel pump startup and coastdown transients, and (right) integral worth of the regulating control rod.[25]

### II.B.2. Uncertainty in Experimental Data

The system response to the pump transient tests was measured in terms of control rod movement that attempted to keep the power level constant. The reactivity response can be calculated using the integral control rod worth curve to transform the rod positions to reactivity units. The MSRE had two control rod position indicators.[27] The coarse indicator rotated 5 deg per inch of control rod movement. The fine indicator rotated 60 deg per inch and had a sensitivity of 0.05 in. A third position indicator was used to measure the relative position of the rod compared to the thimble by measuring the air pressure drop across a built-in flow restrictor.

A second source of uncertainty in the measured data was the response time in the flux-servo controller. The uncertainty sources in the flux servo controller response were the detector dead time and the delay time of the servo motor. These response times were much smaller than the time interval for the recorded measurements (1 s) and were likely to have had a minimal effect on the measured response. Finally, the control rod had a maximum speed of 0.5 in./s (1.27 cm/s). This limitation on the reactivity insertion rate was expected to cause overshooting in the reactivity insertion.[9]

The differential worth measurement of the regulating rod was obtained using the period measurements method at different $^{235}U$ loadings for the stationary fuel.[25] The integral worth curve of the regulating control rod was then obtained by integrating the differential worth curve. Following the period measurements, rod drop measurements were conducted to check the self-consistency of the rod worth measurements. All rod drop measurements were within the 5% band of self-consistency with the rod calibration results.

To estimate an upper and lower bound of the reactivity response during the pump transient test, the uncertainty in the control rod position indicator and the uncertainty in the rod worth curve were considered. A sampling-based approach was used to calculate the standard deviation, which was used as an estimation of the uncertainty interval.[30] The calculation procedure was follows:

1. For each measured rod position, 2000 samples were drawn from a normal distribution with a mean of the measured position and a standard deviation of 0.01 in. (the reported uncertainty in rod position indicator[25]).

2. For each sample, the integral worth curve was used to calculate the reactivity worth at this position.

3. For each value of the reactivity worth values, 2000 samples were drawn from a normal distribution with a mean of the reactivity worth calculated from the integral curve + 1% and a standard deviation of 1% of the mean.

TABLE III

Mean and Estimated STD in the Transient Flow Rate During the Flow Transient Tests

| Coastdown Flow Rate | | | Startup Flow Rate | | |
|---|---|---|---|---|---|
| Time (s) | Mean | STD | Time (s) | Mean | STD |
| 0 | 1 | 0 | 0 | 0 | 0 |
| 1.212 | 0.931 | 0.011 | 0.606 | 0.061 | 0.003 |
| 2.424 | 0.676 | 0.030 | 1.212 | 0.387 | 0.017 |
| 3.636 | 0.445 | 0.031 | 1.818 | 0.638 | 0.022 |
| 4.848 | 0.283 | 0.027 | 2.424 | 0.801 | 0.02 |
| 6.061 | 0.178 | 0.022 | 3.03 | 0.895 | 0.014 |
| 7.273 | 0.124 | 0.017 | 3.636 | 0.946 | 0.009 |
| 8.485 | 0.094 | 0.016 | 4.242 | 0.972 | 0.006 |
| 9.697 | 0.074 | 0.017 | 4.848 | 0.986 | 0.003 |
| 10.909 | 0.063 | 0.019 | 5.455 | 0.993 | 0.002 |
| 12.121 | 0.056 | 0.020 | 6.061 | 0.996 | 0.001 |
| 13.333 | 0.053 | 0.020 | 6.667 | 0.998 | 0.001 |
| 14.545 | 0.051 | 0.018 | 7.273 | 0.999 | 0 |
| 15.758 | 0.049 | 0.017 | 7.879 | 1 | 0 |
| 16.97 | 0.047 | 0.016 | 8.485 | 1 | 0 |
| 18.182 | 0.045 | 0.015 | 9.091 | 1 | 0 |
| 19.394 | 0.044 | 0.015 | 9.697 | 1 | 0 |
| 20.000 | 0.042 | 0.014 | 10.000 | 1 | 0 |

4. Now for each measured position, there were 4 million samples drawn from the distribution of the rod position and worth curve. The mean of these all samples at each time step was used as the best estimate of the reactivity worth, and the standard deviation was used as an estimation of the uncertainty in this response. The reactivity change was calculated by subtracting the reactivity worth corresponding to the initial position for the startup test from all the following points. The uncertainty in the reactivity change was then calculated as $\sqrt{\sigma_0^2 - \sigma_i^2}$, where $\sigma_i$ is the standard deviation of the reactivity worth for the $i$'th point.

Following the estimation of the uncertainty in the experimental measurements, the identified uncertainties in the test parameters were propagated to the reactivity through 4000 evaluations of the computational model described in Sec. IV. The standard deviation of this sample was combined with the experimental uncertainty to provide an overall estimation of the benchmark uncertainty. Figures 4 and 5 show the best estimate of the reactivity responses and the estimated 1σ uncertainty associated with them for the pump startup and pump coastdown transients, respectively. The number below each point refers to the best estimate of reactivity and the number above each point is the estimated 1σ uncertainty.

## III. MATHEMATICAL MODELS

Circulating fuel in MSRs requires the simultaneous modeling of the neutronics and fluid flow to capture the strong coupling between the two phenomena and accurately simulate system performance. The neutronics behavior can be modeled using the multigroup neutron diffusion model coupled with the mass balance of DNP. The standard multigroup neutron diffusion equation is given by

$$\frac{1}{v_g}\frac{\partial \phi_g}{\partial t} = \nabla \cdot D_g \nabla \phi_g - \Sigma_{r,g}\phi_g + \chi_{pg}(1-\beta)\sum_{g'=1}^{G} \nu_{g'}\Sigma_{f,g'}\phi_{g'} + \sum_{g' \neq g}^{G} \Sigma_{s,g' \to g}\phi_{g'} + \sum_{i=1}^{I} \chi_{di,g}\lambda_i C_i \quad , \tag{1}$$

where

subscript $g$ = energy group number
$\phi$ = neutron flux
$v$ = neutron speed

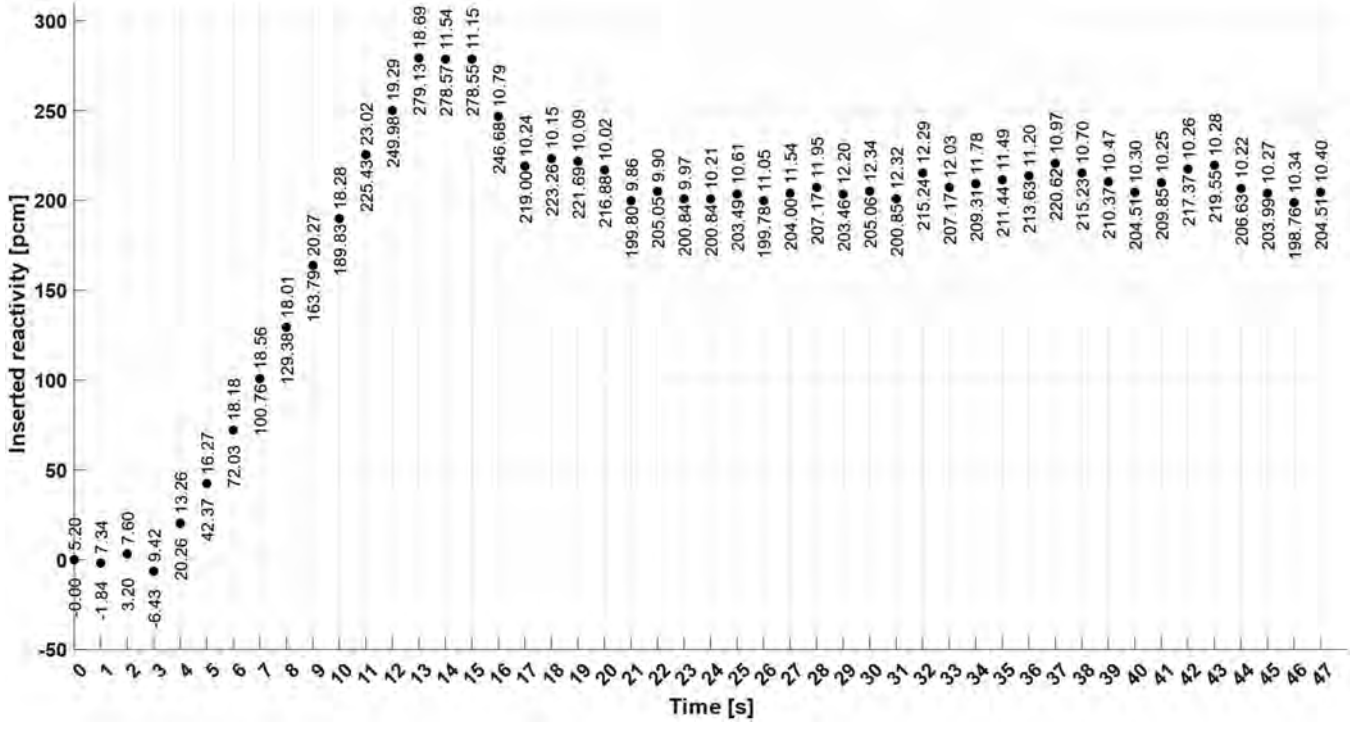


Fig. 4. Best estimate of the reactivity worth of the control rod positions and the overall 1σ uncertainty during the pump startup test.

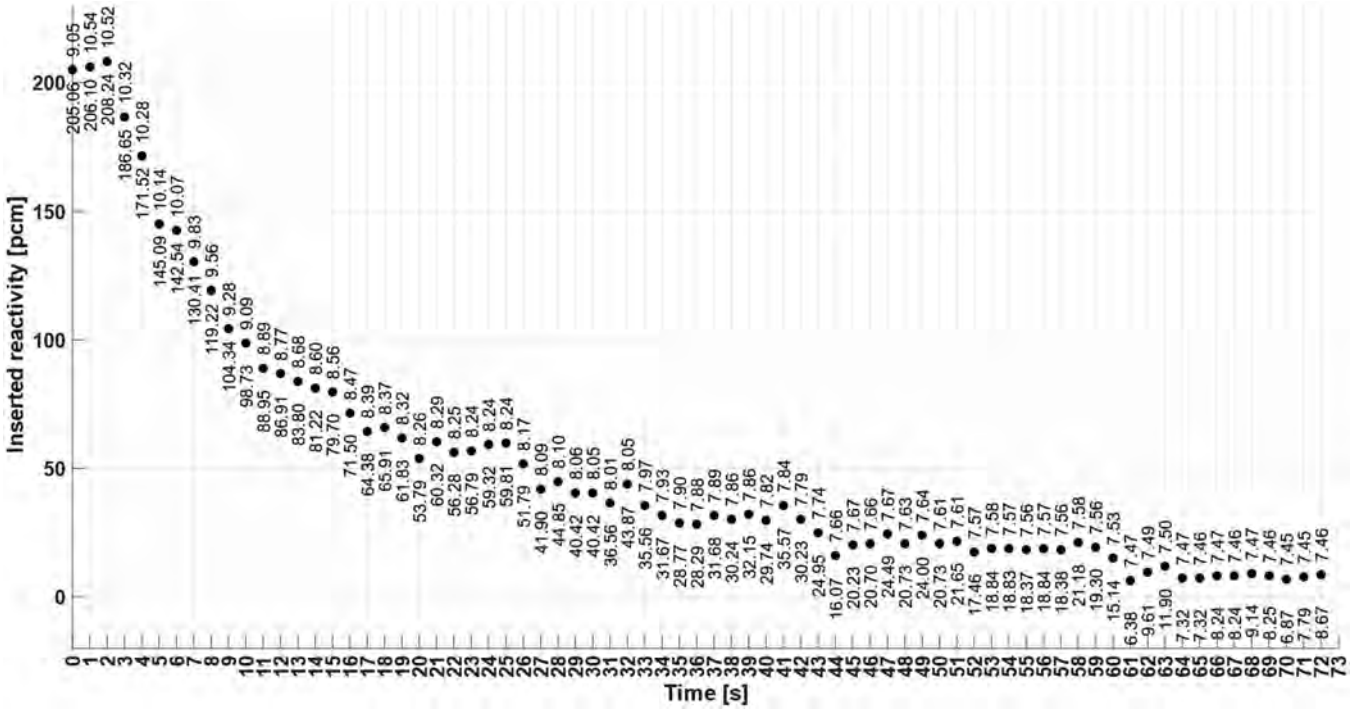


Fig. 5. Best estimate of the reactivity worth of the control rod positions and the overall 1σ uncertainty during the pump coastdown test.

$D$ = neutron diffusion coefficient

$\Sigma_r$ = removal cross section

$\chi_p$ = emission spectrum for prompt neutrons

$\beta$ = total delayed neutron fraction (DNF)

$\Sigma_f$ = fission cross section

$\Sigma_{s,g'\to g}$ = cross section for scattering from group $g'$ to group $g$

$\chi_{di}$ = emission spectrum of delayed neutrons from the $i$'th DNP group

$\lambda_i$ = decay constant of the $i$'th DNP group

$C_i$ = concentration of the $i$'th DNP group ($m^{-3}$).

The DNP concentration for a circulating medium is governed by the mass balance equation given by the advection-diffusion model

$$\frac{\partial C_i}{\partial t} + \nabla \cdot [\mathbf{U}C_i] = \nabla \cdot (D_i \nabla C_i) + \beta_i \sum_{g'=1}^{G} \nu_{g'} \Sigma_{f,g'} \phi_{g'} - \lambda_i C_i \quad , \qquad (2)$$

where

subscript $i$ = DNP group

$\mathbf{U}$ = intrinsic velocity of the circulating fuel

$D_i$ = diffusion coefficient of the $i$'th DNP group

$\beta_i$ = DNFfor the $i$'th DNP group.

The motion of viscous fluid is generally described by Navier-Stokes (N-S) equations, which are a set of nonlinear partial differential equations expressing the mass and momentum balance of the flow system.[31] For the single-phase flow, the N-S equations have the form

$$\frac{\partial \rho}{\partial t} + \nabla \cdot (\rho \mathbf{U}) = 0 \qquad (3a)$$

$$\rho \frac{\partial \mathbf{U}}{\partial t} + \rho(\mathbf{U} \cdot \nabla)\mathbf{U} = -\nabla p + \mu \nabla^2 \mathbf{U} + \mathbf{F} \quad , \qquad (3b)$$

where

$\mathbf{U}$ = velocity field

$\rho$ = density

$p$ = pressure

$\tau$ = viscous stress tensor

$\mu$ = dynamic viscosity

$\mathbf{F}$ = body force vector.

The direct solution of the neutronics model coupled with the N-S equations [i.e., computational fluid dynamics (CFD) equations] for nuclear reactor systems is challenging due to the large scale and the complexity of the reactor systems. The application of the CFD method for modeling fluid flow and heat transfer phenomena in nuclear reactors is currently receiving great attention thanks to the recent developments in high-performance computing technology.[32]

Traditionally, the simulation of nuclear reactor systems involved either the use of system-level codes[33] or the porous medium approximation.[34] The system-level codes, such as RELAP5[35] and SAM,[22] employ a homogenized, lumped, or 1D representation of the system. These codes have been developed for decades and are widely used in steady-state and transient simulations of nuclear reactors.

The porous medium method approximates the fine details of the geometry as a homogeneous porous medium, and thus provides an intermediate fidelity between the detailed CFD and the system-level analysis. The approach is based on volume averaging of the conservative quantities and on using closure relations for the interactions of fluid with the substructure. Coase-mesh CFD has been adopted by several modern thermal-hydraulic codes, including the MOOSE-based code Pronghorn,[36] the open-source code GeN-Foam,[37] and GOTHIC.[11]

## III.A. SYSTEM-LEVEL MODEL

System-level codes are computationally efficient tools that use simplified forms of the conservation equations and empirical closure relations. The applications of system-level codes include safety analyses, designs of new systems, design and interpretation of experimental programs, and licensing.[33] A 1D multigroup neutron diffusion model can be obtained by integrating the flux and DNP over the transverse direction. In such a case, a special treatment is required for neutron leakage in the radial direction.

In our previous work,[38] the detailed derivation of the 1D leakage-corrected neutron diffusion model was discussed. The 1D transport equation for DNP can be derived by integrating the mass balance equation over the direction transverse to the flow direction. The 1D presentation of Eq. (2) takes the form

$$A\frac{\partial C_i}{\partial t}+\nabla\cdot[AuC_i]=\nabla\cdot(D_i\nabla AC_i)+A\beta_i\sum_{g'=1}^{G}\nu_{g'}\Sigma_{f,g'}\phi_{g'}-\lambda_i AC_i \quad , \tag{4}$$

where $A$ is the flow area and the intrinsic velocity $\mathbf{U}$ is replaced with the area averaged velocity $u$.

In many practical applications in nuclear reactors, it is reasonable to use a 1D model for flow in channels where the velocity is averaged over the flow cross section. Such a model can be derived from the N-S equations by assuming negligible motion in the transverse direction. The 1D model for flow in channels can be written in the form[39]

$$A\frac{\partial \rho}{\partial t}+\frac{\partial(A\rho u)}{\partial z}=0 \tag{5a}$$

$$\rho\frac{\partial u}{\partial t}+\rho u\frac{\partial u}{\partial z}=-\frac{\partial p}{\partial z}-f_D\frac{\rho}{2d_h}u|u|+\mathbf{F} \quad , \tag{5b}$$

where $f_D$ is the Darcy friction factor and $d_h$ is the hydraulic diameter.

The 1D model has the advantage of efficiently simulating flow phenomena at full scale. The disadvantages of this approach are the loss of information about the transverse flow distribution and the difficulty of casting complex flow geometries into 1D representations.

## III.B. Porous Medium Model

In the porous medium treatment, the complex geometry is simplified by an equivalent homogenized medium with volume-averaged properties. This simplification allows for the use of coarse mesh to represent complex systems. Geometry homogenization is a typical practice in generating the cross-section parameters for the neutron diffusion equation.

For the fluid flow model, the Darcy velocity (i.e., the velocity averaged over the medium volume) is used to describe the flow field in the porous medium. The relation between the Darcy velocity and the intrinsic velocity is given by

$$\mathbf{u}=\varepsilon\mathbf{U} \quad . \tag{6}$$

The proportionality constant is the medium porosity $\varepsilon$, which is defined as the fraction of the total volume that is occupied by the fluid phase. In the porous medium

treatment, the DNPs are present only in the fluid phase (i.e., porous volume). Thus Eq. (2) is multiplied by the porosity $\varepsilon$,

$$\varepsilon\frac{\partial C_i}{\partial t}+\nabla\cdot[\mathbf{u}C_i]=\varepsilon\nabla\cdot(D_i\nabla C_i)+\varepsilon\beta_i\sum_{g'=1}^{G}\nu_{g'}\Sigma_{f,g'}\phi_{g'}-\varepsilon\lambda_i C_i \quad , \tag{7}$$

where $C_i$ is the fluid phase concentration (i.e., per unit volume of the fluid phase).

Darcy's law of flow in porous media is an empirical relation that states that the steady-state flow rate is proportional to the applied pressure gradient.[40] The general form of Darcy's law is given by

$$\mathbf{u}=\mu^{-1}\mathbf{K}\cdot\nabla p \quad , \tag{8}$$

where $\mu$ is the dynamic viscosity and $\mathbf{K}$ is the permeability tensor, which is a property of the porous medium representing the ability to conduct flow.[41] It is important to note that the velocity given by Eq. (8) is the Darcy velocity (i.e., the velocity averaged over the medium volume). The mass and momentum conservation of fluid flowing in porous medium following Darcy's law is given by

$$\varepsilon\frac{\partial\rho}{\partial t}+\nabla\cdot(\rho\mathbf{u})=0 \tag{9a}$$

$$\frac{\rho}{\varepsilon}\frac{\partial\boldsymbol{u}}{\partial t}+\frac{\rho}{\varepsilon^2}(\boldsymbol{u}\cdot\nabla)\boldsymbol{u}=-\nabla p-\mu\boldsymbol{K}^{-1}\boldsymbol{u}+\boldsymbol{F}\ . \tag{9b}$$

Darcy's law holds for sufficiently small velocity (Reynolds number less than 1).[40] Forchheimer corrected for the deviation from the Darcy's law at higher Reynolds numbers by adding a quadratic drag term.[40] The Brinkman's equation is considered an extension to Darcy's law, where an additional term is added to the momentum equation, similar to the Laplacian term in the N-S equations. The conservation equations under Brinkman's law are given by[40]

$$\varepsilon\frac{\partial\rho}{\partial t}+\nabla\cdot(\rho\mathbf{u})=0 \tag{10a}$$

$$\frac{\rho}{\varepsilon}\frac{\partial\mathbf{u}}{\partial t}+\frac{\rho}{\varepsilon^2}(\mathbf{u}\cdot\nabla)\mathbf{u}=-\nabla p-\mu\mathbf{K}^{-1}\mathbf{u}+\widetilde{\mu}\nabla^2\mathbf{u}-c_F\rho\mathbf{K}^{-1/2}|\mathbf{u}|\mathbf{u}+\mathbf{F} \quad , \tag{10b}$$

where $\widetilde{\mu}$ is an effective viscosity and is geometry independent, and $c_F$ is a dimensionless form-drag constant. The effective viscosity is typically taken to be equal to the fluid viscosity ($\widetilde{\mu}=\mu$). It is worth noting that as the permeability tensor reaches zero ($\mathbf{K}\to 0$) the Brinkman's equation is reduced to Darcy's equation. On the other hand, Brinkman's equation is reduced to the N-S equations as the permeability tensor reaches infinity ($\mathbf{K}\to\infty$).

Finally, the inertial term $(\mathbf{u}\cdot\ \ )\mathbf{u}$ in Eq. (10) is typically ignored for the following reasons[40]: (1) it is inconsistent with the slip boundary condition, (2) in the presence of a fixed solid matrix, the fluid particle does not generally retain momentum flowing from point to point, and (3) the inertial term is generally smaller than the quadratic drag term $c_F\rho\mathbf{K}^{-1/2}|\mathbf{u}|\mathbf{u}$. Neglecting the inertial term, the Brinkman's equation takes the form

$$\varepsilon\frac{\partial\rho}{\partial t}+\nabla\cdot(\rho\mathbf{u})=0 \tag{11a}$$

$$\frac{\rho}{\varepsilon}\frac{\partial\mathbf{u}}{\partial t}=-\nabla p-\mu\mathbf{K}^{-1}\mathbf{u}+\mu\nabla^2\mathbf{u}-c_F\rho\mathbf{K}^{-1/2}|\mathbf{u}|\mathbf{u}+\mathbf{F}\ . \tag{11b}$$

## III.C. NEUTRONICS TRANSIENT MODEL

For the transient under consideration, the total fission power was assumed to be constant, and the simulation could be simplified using the improved quasi-static approach.[42,43] Under the assumption that the flux shape is weakly dependent on time, the flux can be factorized into shape and amplitude functions,

$$\phi_g(\mathbf{r},t)=P(t)\varphi_g(\mathbf{r},t)\ . \tag{12}$$

Substituting it into Eq. (1) and introducing the multiplication factor $k_{eff}$, which Eq. (12) required to correct for criticality in steady state, gives

$$\frac{1}{v_g}\left(\varphi_g\frac{\partial P}{\partial t}+P\frac{\partial\varphi_g}{\partial t}\right)=\nabla\cdot D_g\nabla P\varphi_g-\Sigma_{r,g}P\varphi_g+\frac{\chi_{pg}(1-\beta)}{k_{eff}}\sum_{g'=1}^{G}\nu_{g'}\Sigma_{f,g'}P\varphi_{g'}+\sum_{g'\neq g}^{G}\Sigma_{s,g'\to g}P\varphi_{g'}+\sum_{i=1}^{I}\chi_{d,i,g}\lambda_i C_i\ . \tag{13}$$

For the special case in which the total power is constant, Eq. (13) is reduced to

$$\frac{1}{v_g}\frac{\partial \varphi_g}{\partial t} = \nabla \cdot D_g \nabla \varphi_g - \Sigma_{r,g}\varphi_g + \frac{\chi_{pg}(1-\beta)}{k_{eff}} \sum_{g'=1}^{G} \nu_{g'}\Sigma_{f,g'}\varphi_{g'} + \sum_{g' \neq g}^{G} \nu_{s,g' \to g}\varphi_{g'} + \frac{1}{P}\sum_{i=1}^{I} \chi_{d,i,g}\lambda_i C_i \quad (14)$$

where $k_{eff}$ is treated as a time-dependent parameter that can be calculated as the ratio of the fission power at some time step to the initial fission power,

$$k_{eff}(t_i) = k_{eff}^0 \frac{\int_V \sum_{g'=1}^{G} \nu_{g'}\Sigma_{f,g'}\varphi_{g'}(t_i)}{\int_V \sum_{g'=1}^{G} \nu_{g'}\Sigma_{f,g'}\varphi_{g'}(t_0)} \quad , \quad (15)$$

where $k_{eff}^0$ is $k_{eff}$ at $t = 0$.

In a similar manner, the DNP equations become

$$\frac{\partial C_i}{\partial t} + \nabla \cdot [\mathbf{U}C_i] = \nabla \cdot (D_i \nabla C_i) + \frac{\beta_i}{k_{eff}} \sum_{g'=1}^{G} \nu_{g'}\Sigma_{f,g'}P\varphi_{g'} - \lambda_i C_i \quad . \quad (16)$$

In this treatment, the dynamical weighting factor $k_{eff}$ mimics the addition or the withdrawal of reactivity to maintain the power level.

### III.D. Diffusion of the DNP

The diffusion coefficient of the DNP accounts for both the molecular and turbulent diffusive effects in the flowing fluid.[44] It can be defined as

$$D_i = D_{c,i} + D_T \quad , \quad (17)$$

where $D_{c,i}$ is the molecular diffusion coefficient, and $D_T$ is the turbulent diffusion coefficient given as the ratio between the eddy viscosity $\upsilon_T$ and the turbulent Schmidt number of the fluid.

Molecular diffusion typically has a smaller magnitude compared to the advection term and turbulent diffusion.[45] Moreover, due to the lack of data on the turbulent mass transport, a sensitivity study for the effect of the turbulent Schmidt number on the effective DNF was carried out in Ref. [46]. The results indicated that changing the turbulent Schmidt number over two orders of magnitude resulted in about a 20 pcm (1 pcm = $10^{-5}$) change in the effective DNF.

In the current work, no turbulent modeling was considered for the fluid flow. The effect of turbulent diffusion was studied using the system-level model through the Taylor correlation,[39] as discussed in Sec. IV.B.

## IV. SYSTEM-LEVEL BENCHMARK RESULTS

The MSRE fuel circulation loop was cast into a 1D representation where each component was represented by a 1D segment with a length equal to the physical length of the component. The effective cross-sectional area of each component was calculated by dividing the salt volume by the length to preserve the residence time. The geometrical parameters of the 1D model are given in Table IV. Note that the residence times given in Table IV were calculated at the nominal flow rate (1200 gpm). The geometry and flow network of the 1D model are shown in Fig. 6. No bypass flow was considered in the 1D model.

The 1D computational models given by Eqs. (4), (5), and (14) were implemented in COMSOL Multiphysics,[47] and the resultant fully coupled system was solved simultaneously. The neutron diffusion model given by Eq. (14) was solved for the lower head, core, and upper head regions subject to the albedo boundary condition. The number of elements for the neutron diffusion equation (core region) was 51, and the number of elements for the fluid flow model (fuel loop) was 172. More details about the 1D model implementation can be found in Ref. [38].

The simulation started by solving Eq. (14) in eigenvalue mode to obtain the stationary flux distribution. A pseudo-transient step was then used to obtain the initial concentration of the DNP. After obtaining the initial conditions of the system, the pump startup test was initiated by increasing the flow rate in the loop according to the regenerated flow rate (see Table III). During the transient, the total power was kept constant through the dynamic multiplication factor $k_{eff}$ defined by Eq. (15). After the system reached the steady state, the coastdown transient was initiated by reducing the flow rate in the loop according to the regenerated flow rate. The total power was kept constant in a similar manner to the startup case.

In this treatment, the changes in $k_{eff}$ were equivalent to the control rod movement attempting to keep the power constant. The reactivity inserted to maintain a constant power can be calculated using

TABLE IV

Geometrical Parameters of the 1D Model of the MSRE Fuel Circulation Loop

| Component | Length (m) | Effective Flow Area ($m^2$) | Volume ($m^3$) | Residence Time (s) |
|---|---|---|---|---|
| Core | 1.67 | 0.425 | 0.7086 | 9.4 |
| Upper plenum | 0.35 | 0.850 | 0.2973 | 3.9 |
| Line 100 horizontal | 1.83 | 0.013 | 0.0236 | 0.3 |
| Line 100 vertical | 0.81 | 0.045 | 0.0365 | 0.5 |
| Pump | 0.57 | 0.045 | 0.0255 | 0.3 |
| Line 101 (pump to HX) | 1.70 | 0.013 | 0.0220 | 0.3 |
| HX | 2.44 | 0.071 | 0.1729 | 2.3 |
| Line 102 (HX to vessel) | 4.65 | 0.013 | 0.0600 | 0.8 |
| Distributor + downcomer | 6.28 | 0.044 | 0.2751 | 3.6 |
| Lower plenum | 0.34 | 0.827 | 0.2834 | 3.8 |
| Total | | | 1.9057 | 25.2 |

$$\rho_{in}(t_i) = -\Delta\rho = \frac{k^0_{eff} - 1}{k^0_{eff}} - \frac{k_{eff}(t_i) - 1}{k_{eff}(t_i)} = \frac{k_{eff}(t_i) - k^0_{eff}}{k_{eff}(t_i) \times k^0_{eff}} \quad . \tag{18}$$

The cross sections and DNP data for the neutronics model were generated using the Serpent model based on the MSRE static benchmark[48] and the nuclear library ENDF/B-VII.1. A detailed description of the homogenized cross-section generation for the 1D model for the MSRE can be found in Ref. [38].

The following subsections discuss the effects of various modeling choices on the calculated reactivity response.

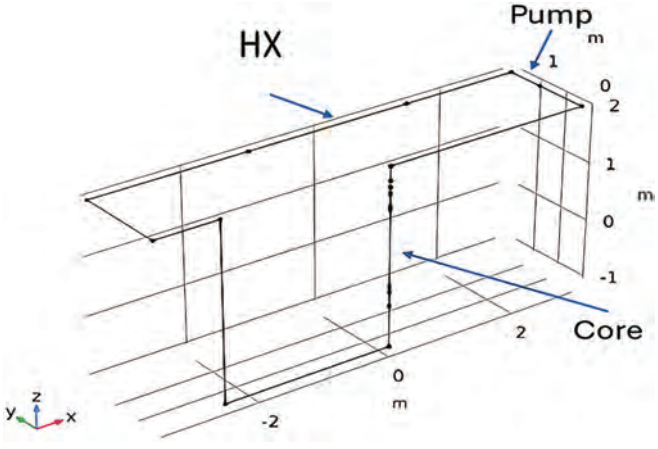


Fig. 6. Schematic geometry of the system-level model.

## IV.A. Effect of Neutron Energy Group Structure

There is no generally accepted group structure for the multigroup neutron diffusion equation for MSRs. In our previous study,[38] we showed that an energy structure with eight groups achieved the highest accuracy for the steady-state, stationary, 1D model of the MSRE. The group boundaries of the eight-group (8G) energy structure were set equidistantly on the lethargy scale and are given in Table V. In the current work, two sets of multigroup cross sections are generated using Serpent. The first set used the standard two-group (2G) energy structure with a thermal energy cutoff at 0.625 eV and the second set used the 8G energy structure. Both sets were used to simulate the pump transient test to evaluate the effect of energy discretization on the transient modeling of the MSRE. A detailed description of the cross-section generation model, along with the 2G cross sections, are provided in Ref. [38].

For the 2G energy structure, all neutrons were generated in the fast group. This did not take into consideration the fact that delayed neutrons are generated with a lower energy spectrum compared to the prompt neutrons, as shown in Fig. 7 for the thermal fission of $^{235}U$. This makes the contribution of delayed neutrons of relatively higher importance in thermal spectrum reactors. In this case, the adjoint-weighted DNF should be used instead of the forward-weighted DNF to account for the higher importance of delayed neutrons. For the 8G case, this effect was accounted for through the groupwise yield $\chi_{p,g}$ and $\chi_{d,i,g}$. Thus, the forward-weighted DNF should be used. The forward-weighted and the adjoint-weighted DNF, generated using Serpent, are given in Table VI.

TABLE V

Group Boundaries for the 8G Energy Structure

| Group | 1 | 2 | 3 | 4 | 5 | 6 | 7 | 8 |
|---|---|---|---|---|---|---|---|---|
| Upper energy boundary (MeV) | 1.96E+1 | 4.98E-1 | 5.00E-3 | 6.79E-5 | 6.16E-6 | 1.48E-6 | 5.00E-7 | 5.80E-8 |

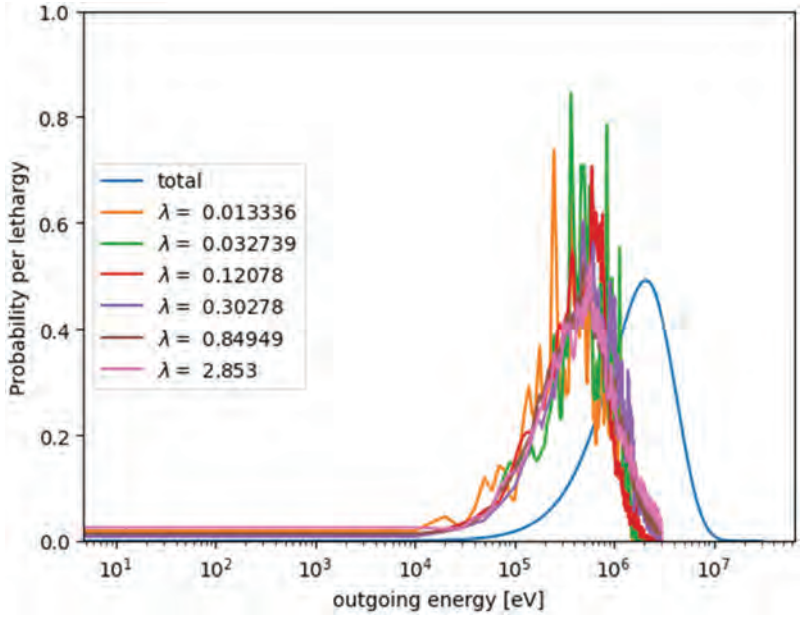


Fig. 7. Energy spectrum $\chi(E)$ of neutrons produced by thermal fission in $^{235}$U from the ENDF/B-VIII.0 library.[49]

TABLE VI

Delayed Neutron Parameters from the ENDF/B-VII.1 Library

| $i$ | Half-Life, $t_{\frac{1}{2}}$(s) | Decay Constant, $\lambda(s^{-1})$ | Forward-Weighted Fractions, $\beta$ | Adjoint-Weighted Fractions, $\beta_{eff}$ |
|---|---|---|---|---|
| 1 | 51.96 | 0.01334 | 0.000224 | 0.000225 |
| 2 | 21.17 | 0.03274 | 0.001167 | 0.001249 |
| 3 | 5.74 | 0.12078 | 0.001113 | 0.001170 |
| 4 | 2.29 | 0.30282 | 0.002497 | 0.002671 |
| 5 | 0.82 | 0.84966 | 0.001026 | 0.001093 |
| 6 | 0.24 | 2.85376 | 0.000427 | 0.000468 |
| Total | – | – | 0.006455 | 0.006877 |

For both cases, the molecular diffusion coefficient of DNP was assumed to be constant and set with the commonly used value of $5 \times 10^{-9}$ m$^2$/s,[50] while the turbulent diffusion was neglected. The simulated reactivity responses using the two multigroup energy structures compared with the experimental data for both the pump startup and coastdown transients are shown in Fig. 8. These results first suggest that the 2G structure with effective DNF is nearly equivalent to the 8G structure in predicting the reactivity changes due to changes in the delayed neutron source for the MSRE. Henceforth, the 2G energy structure was primarily used throughout the rest of the work.

For the startup transient, the model predictions generally were in good agreement with the measurements. Especially,

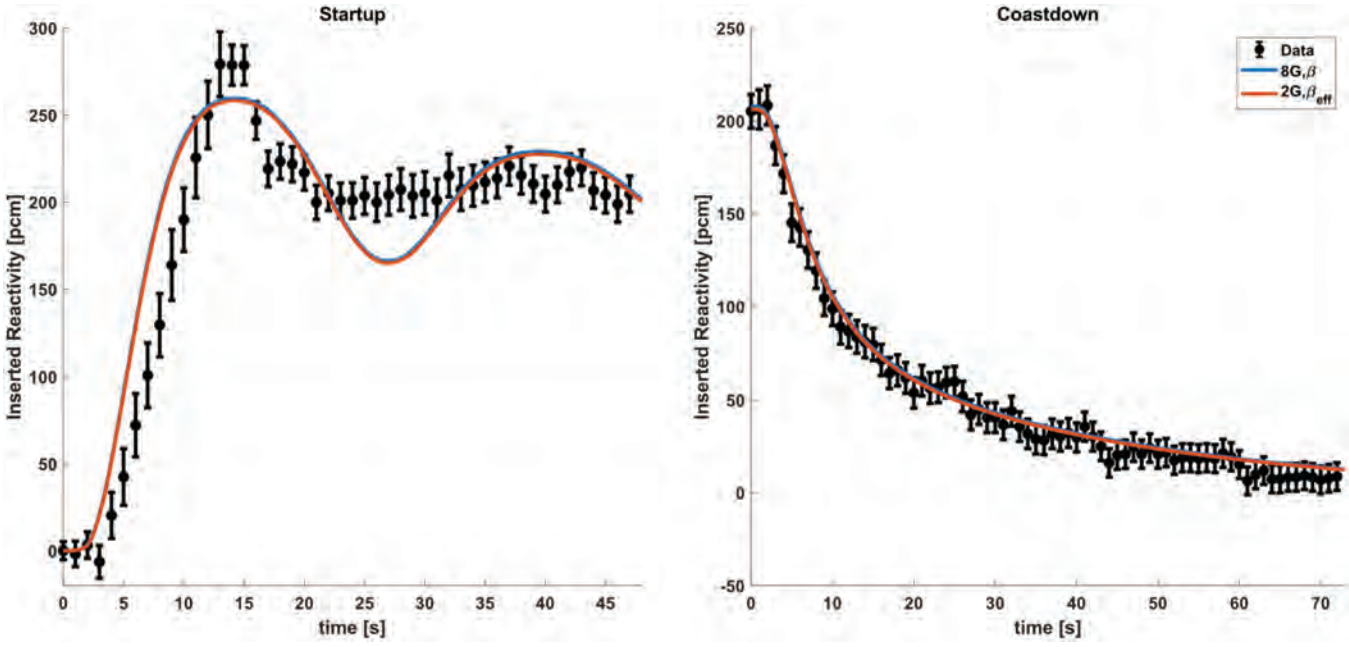


Fig. 8. Calculated reactivity response for the pump transient tests using the 1D model for two different group structures.

the model converged to a steady-state reactivity that was in good agreement with the experimental steady-state data. However, the rate of reactivity insertion at the initial phase of the startup transient was slightly overestimated up to 10s into the transient. This was primarily attributed to the result of neglecting bypass flows in the 1D model. Bypass flows in the MSRE vessel would reduce the average flow speed in the core, which would reduce the rate of DNP drift, and consequently, the rate of reactivity insertion.

Another possible source of discrepancy was the neglection of the radial distribution of flow and DNP concentrations in the 1D model. Additionally, the model predictions exhibited larger reactivity oscillations compared to the experimental data. The oscillations had a periodic time of ~25 s, which was about the fuel circulation time. The reactivity oscillations were associated with the recirculation of the salt portion that initially filled the core with higher concentrations of DNP. The dispersion mechanisms of the higher concentration portion were molecular diffusion and dispersion due to flow mixing. Neglecting the turbulent diffusion coefficient in the simulation caused the higher concentration portion to dissipate at a slower rate, which in turn resulted in stronger reactivity oscillations.

On the other hand, the coastdown test started from a flowing condition where the salt was well mixed and there was no portion of the salt that had a higher DNP concentration. Under these conditions, the reactivity response was much smoother, with nearly no oscillations. As a result, the predicted response for the coastdown transient was in excellent agreement with the experimental data. The mean absolute error in the model predictions compared to the experimental data was 21 pcm for the startup transient and 4.6 pcm for the coastdown transient.

## IV.B. Effect of Turbulent Diffusion Coefficient

As shown in Sec. IV.A, the 1D model accurately predicted the reactivity peak as well as the steady-state reactivity. For the startup case, the model overestimated the reactivity oscillations. To understand the effect of turbulent diffusion on the reactivity response, we used the Taylor correlation[51] to account for the DNP dispersion due to flow. For turbulent flow, the Taylor correlation is given by

$$D_T = 10.1 \frac{d_h}{2} u \sqrt{\frac{f_D}{2}} \quad , \tag{19}$$

where $d_h$ is the hydraulic diameter and $f_D$ is the friction coefficient. The Taylor diffusion coefficient corrects for the use of the mean flow speed (i.e., 1D speed) for species transport instead of using the actual flow distribution over the cross section of the flow channel.[52] The effect of correcting the DNP diffusion coefficient by considering the turbulent diffusion term is shown in Figs. 9 and 10.

Figure 9 shows the effect of turbulent diffusion on the reactivity response. The turbulent diffusion correlation had a dampening effect on the reactivity response as

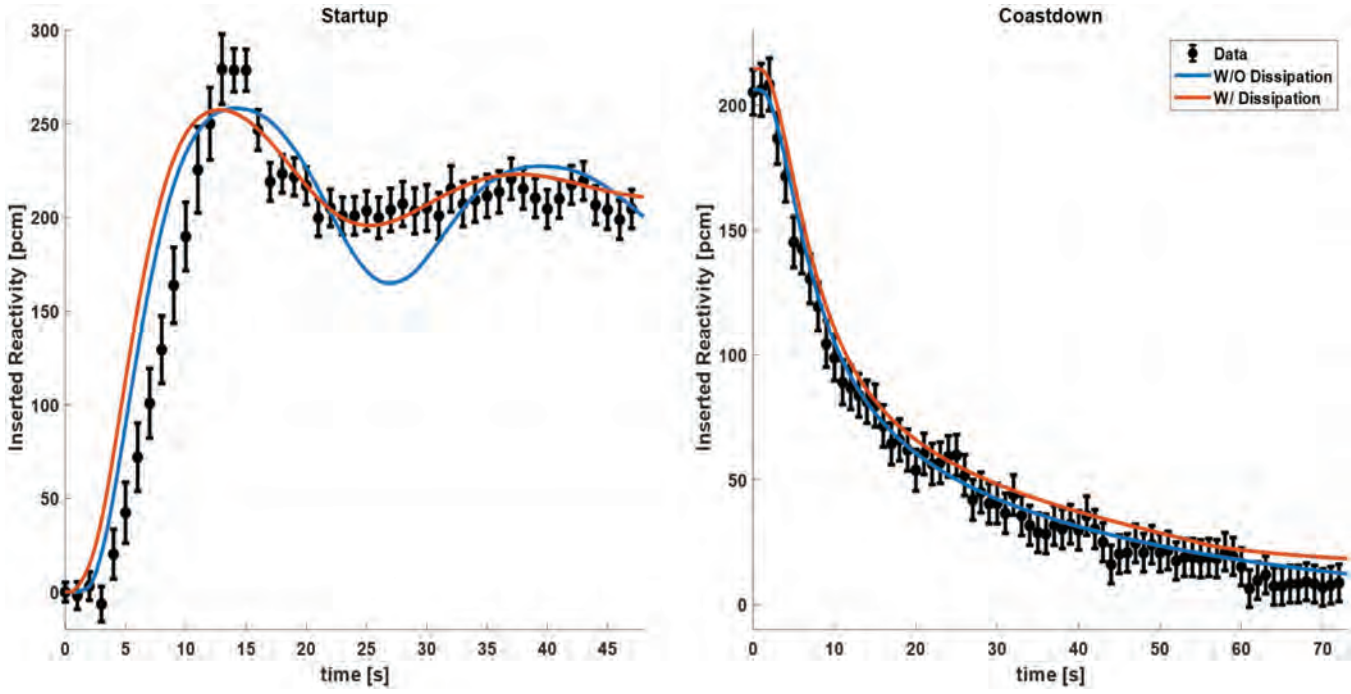


Fig. 9. Calculated reactivity response for the pump transient test for different treatments of the diffusion of the DNPs.

expected. This is explained in Fig. 10, where the oscillations in the total number of DNPs in the core were significantly dampened when adding the turbulent diffusion term. The steady-state reactivity was higher than the case with no turbulent diffusion by about 8 pcm.

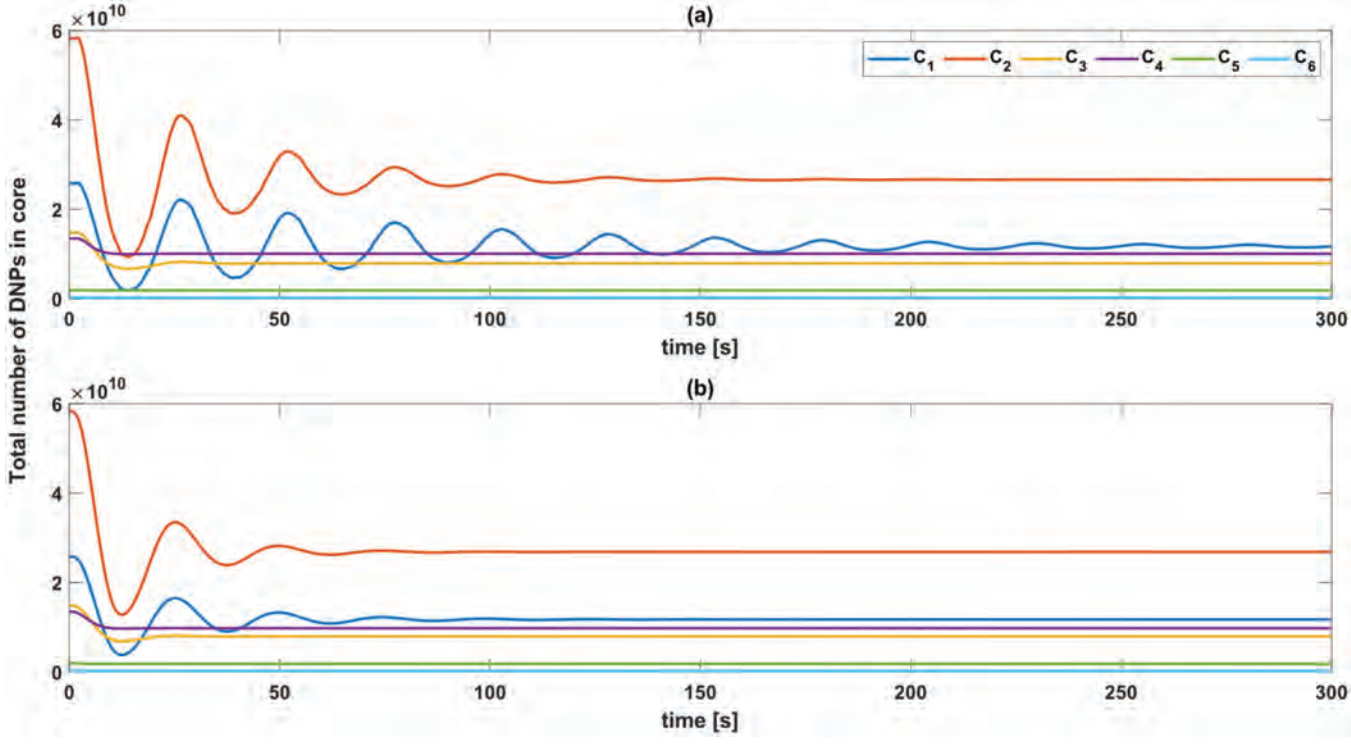


Fig. 10. Total number of DNPs during the pump startup test: (a) with no turbulent diffusion term and (b) using the Taylor correlation.

This increase in the inserted reactivity indicated that the turbulent mixing reduced the effective residence time of DNP due to the additional transport mechanism. This effect also explained the sharper rise in the reactivity response at the start of the test as the DNPs exited the core faster. The rapid rise in the reactivity response compared to the experimental data suggested that using the Taylor correlation for turbulent flow may be not valid at the start of the test when the flow is in the laminar regime.

For the coastdown case, the turbulent diffusion only increased the initial reactivity. These results support the findings in Ref. [46] about the effect of turbulent diffusion on the steady state. The increase in inserted reactivity was caused by enhanced mobility, which caused the DNPs to spend less time in the core. Furthermore, the results showed that turbulent diffusion had a significant impact on the transient response of MSRs.

The mean relative error in the reactivity response for the startup transient was 19 pcm for the turbulent diffusion–corrected model. This was slightly lower than the error for the uncorrected model, which was 21 pcm. Despite capturing the transient very well, the accuracy of the predictions only slightly increased due to the larger error at the start of the test and the 8 pcm increase in steady-state reactivity. For the same reason, the error in the coastdown predictions for the corrected model was 9 pcm compared to 4.6 pcm for the uncorrected model. Although, considering the turbulent diffusion of DNP through the Taylor correlation improved the model capability for predicting the transient response, more studies are needed to determine the accurate molecular diffusion coefficients and turbulent diffusion coefficients for molten salts.

### IV.C. Effect of DNP Group Structure

The most widely used approximation for delayed neutron emission is the six-group (6G) DNP structure. It simplifies delayed neutron data into six average groups that reasonably approximate the behavior of DNP. The 8G DNP structure is a refinement that adds two additional groups to improve accuracy, particularly for the MSRs.[46] To investigate the impact of the DNP structure on the calculated reactivity response in the MSRE pump transients, the results of two distinctive sets of DNP data were compared. The first set was the 6G structure, which was generated using the nuclear data library ENDF/B-VII.1, is shown in Table VI. The second set was the 8 G structure, which was generated using the nuclear data library JEFF-3.2,[53] with the 8G DNP data summarized in Table VII.

The adjoint-weighted DNP fractions were used with the 2G neutron diffusion model to simulate the reactivity response during the MSRE pump transient test. A comparison between the two sets of DNP parameters and the experimental data is shown in Fig. 11. The use of the 8G DNP structure systematically led to an overestimation of the reactivity response when compared to the 6G structure. This was partially explained by the higher total DNP fraction $\beta$ calculated using the JEFF-3.2 library compared to the ENDF/B-VII.1 library. The DNP structure significantly influenced the reactivity magnitude while having a negligible effect on the time response. For the remaining parts of this work, the 6G DNP structure was used.

## V. HIGHER-ORDER BENCHMARK RESULTS

To investigate the spatial effects on the reactivity response to the pump transient test, a higher-order model was used. The geometry of the MSRE reactor vessel from the CAD model[23] was simplified to suit the simulation purposes. These simplifications included replacing the graphite matrix with a cylindrical porous region, removing the strainer at the outlet nozzle, and blocking the bypass slots. A preliminary CFD analysis on the three-dimensional (3D) geometry was conducted to examine the steady-state nominal flow condition in the MSRE.

The mesh used for the CFD analysis, shown in Fig. 12, was generated using ANSYS Fluent. The mesh consisted of 4 million polyhedral cells. The maximum skewness was 0.65. The wall effect on the turbulence boundary layer was neglected, and thus no inflation layers were generated to simplify the mesh and aid convergence. SimpleFOAM, a steady-state solver in OpenFOAM, an open-source CFD software package specifically designed to simulate incompressible, turbulent flow problems, was used for the CFD simulation. OpenFOAM version v2312 was used for these simulations.

The $k-\varepsilon$ turbulence model was used to capture regions with swirls. The graphite matrix was replaced with a porous media, using an explicit porosity source to mimic the flow in the graphite channels by imposing a unidirectional flow. The velocity inlet boundary condition was used for the inlet with a flow rate of 0.074 $m^3/s$ (1200 gpm). The pressure outlet boundary condition was used for the outlet, and the no-slip condition was used for walls. The convergence criteria was set to a tolerance of 1E-6.

The CFD calculation was performed on a Linux cluster using 16 cores over about 24 h. The results of the CFD calculations are shown in Fig. 13. The velocity vectors indicated a predominantly smooth flow along the graphite matrix (porous media) region and the upper plenum. The flow was turbulent in the lower head, which was evident

TABLE VII

Delayed Neutron Parameters from the JEFF-3.2 Library

| $i$ | Half-Life, $t_{\frac{1}{2}}$(s) | Decay Constant, $\lambda(s^{-1})$ | Forward-Weighted Fractions, $\beta$ | Adjoint-Weighted Fractions, $\beta_{eff}$ |
|---|---|---|---|---|
| 1 | 55.60 | 0.01247 | 0.000218 | 0.000238 |
| 2 | 24.50 | 0.02829 | 0.001003 | 0.001047 |
| 3 | 16.30 | 0.04252 | 0.000615 | 0.000651 |
| 4 | 5.21 | 0.13304 | 0.001305 | 0.001434 |
| 5 | 2.37 | 0.29247 | 0.002146 | 0.002277 |
| 6 | 1.04 | 0.66649 | 0.000607 | 0.000649 |
| 7 | 0.42 | 1.63478 | 0.000549 | 0.000577 |
| 8 | 0.20 | 3.5546 | 0.000155 | 0.000168 |
| Total | – | – | 0.006599 | 0.007040 |

by the formation of vortices but got smoothed out once it entered the graphite matrix. The highest flow velocities occurred in the annulus and outlet nozzle.

Due to the large computational cost of the 3D model, it was decided to conduct the neutronics/flow dynamics–coupled calculations for the pump transients using a R-Z 2D geometry by assuming azimuthal symmetry. The validity of this assumption was justified by the axial symmetry of the velocity field at the entrance of the graphite matrix, as shown in Fig. 14. Figure 14(a) shows the velocity field below the supporting grid, which shows the velocity vortices. Figure 14(b) shows the velocity field entering the graphite region, which was almost azimuthally symmetric.

## V.A. R-Z Geometry

Based on the preliminary CFD analysis on the nominal flow conditions of the reactor, a R-Z 2D geometry of the MSRE reactor vessel was used to simulate the pump transient test in this work. The 2D geometry along with the computational mesh for the coupled neutronics and thermal-fluidic calculations is shown in Fig. 15. The mesh, which was used for both the neutronics and thermal-fluidic calculations, consisted of 5607 elements with a minimum quality of 0.1243 and an average quality of 0.7426. The bypass flow from the annulus to the upper head was also considered by creating an opening in the barrier between the two parts, as shown in the magnified

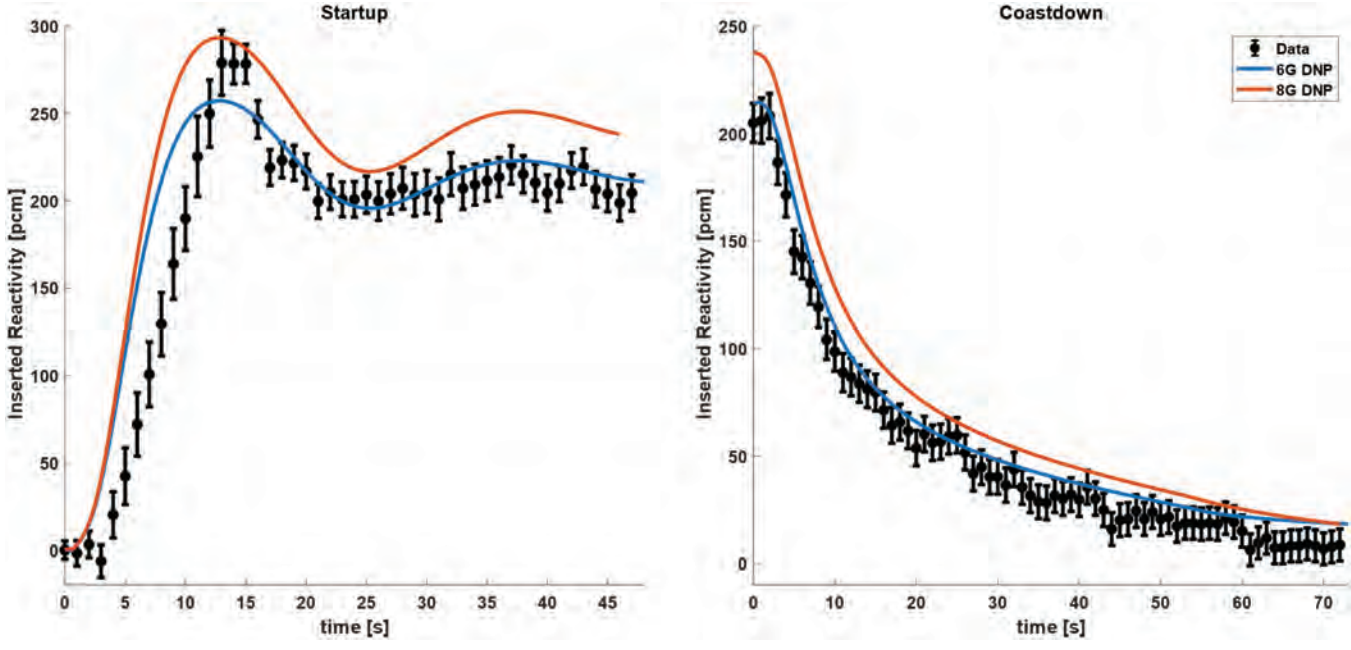


Fig. 11. Calculated reactivity response for the pump transient test for the two sets of DNP group structures.

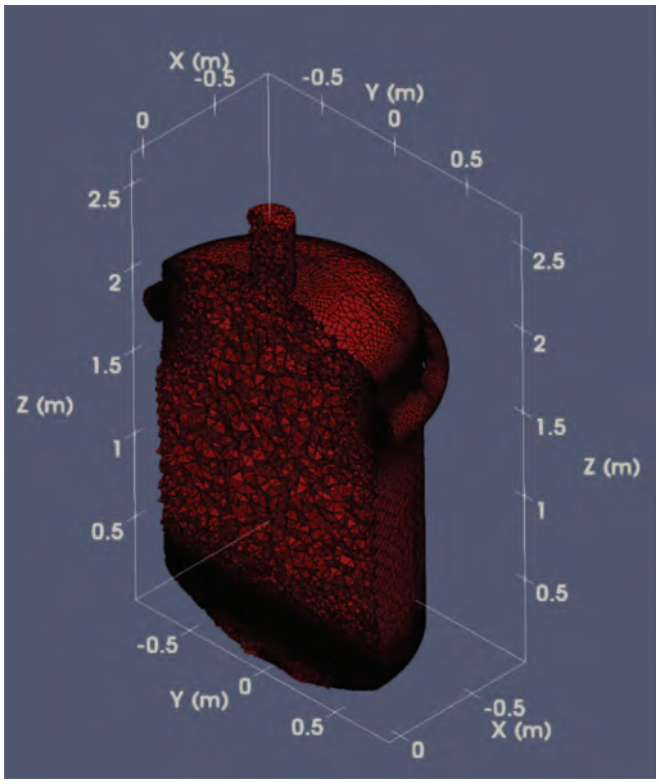


Fig. 12. Mesh for the 3D CFD calculations.

part of Fig. 15. The width of this opening could be adjusted to control the bypass flow rate.

The external components of the primary loop were modeled by extending the outlet nozzle so that the volume of the outlet nozzle became equal to the fuel salt volume in the external loop. The porosity for each region was calculated as the ratio of the salt volume to the geometry volume. The geometrical parameters for each component in the primary loop are provided in Table VIII.

The neutronics/flow models given by Eqs. (7), (11), and (14) were implemented in COMSOL Multiphysics. An iterative approach was employed to solve the coupled system using the segregated solver. The backward differentiation formula solver was used for time stepping. The 2G neutron diffusion model with the adjoint-weighted DNFs was used for neutronics modeling. The fluid flow modeling did not consider turbulent effects; this was justified by the low Reynolds number in the reactor core, which was 1400. Consequently, the turbulent diffusion of the DNP was ignored.

The boundary conditions for the fluid flow model were a predefined mass flow rate at the reactor vessel inlet, open boundary at the end of the outlet nozzle, and no-slip boundary condition for all remaining boundaries. For the neutron diffusion model, the zero incoming current boundary condition was used for all boundaries of the reactor vessel.

For the DNP transport model, a periodic boundary condition was used between the end of the outer loop and the inlet of the reactor vessel, as shown in Fig. 16. The outer loop was simplified as a uniform pipe with a volume equal to the volume of the fuel salt in the external loop (see Fig. 16). Initial conditions for the

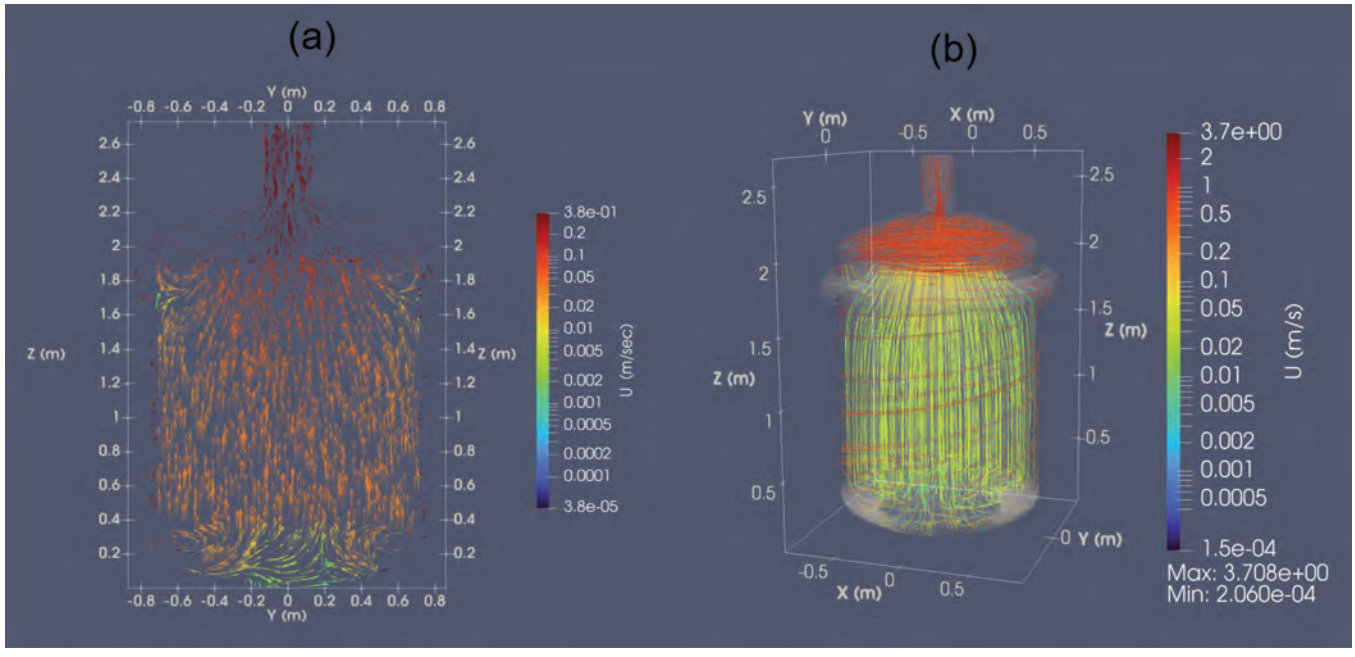


Fig. 13. Velocity field for the 3D CFD calculations: (a) side view of the velocity vector at the center plane of the reactor vessel and (b) flow streamlines.

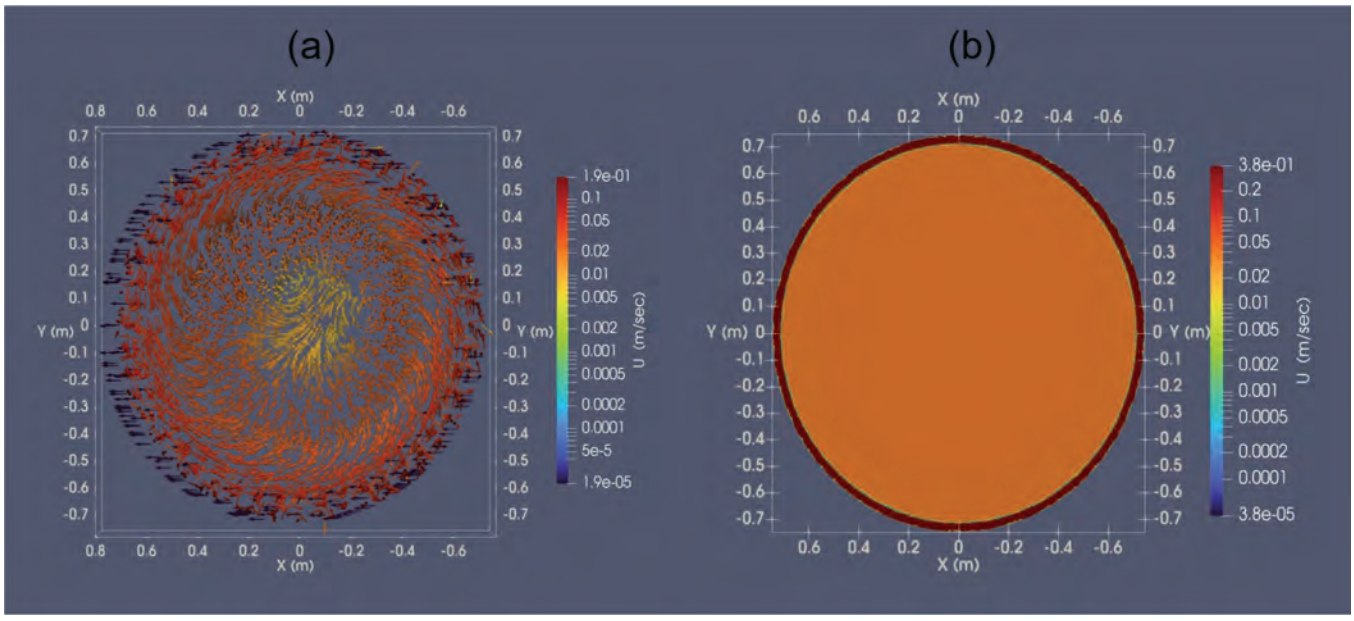


Fig. 14. Top view of the velocity field in the lower plenum: (a) below the support grid and (b) at the core entrance.

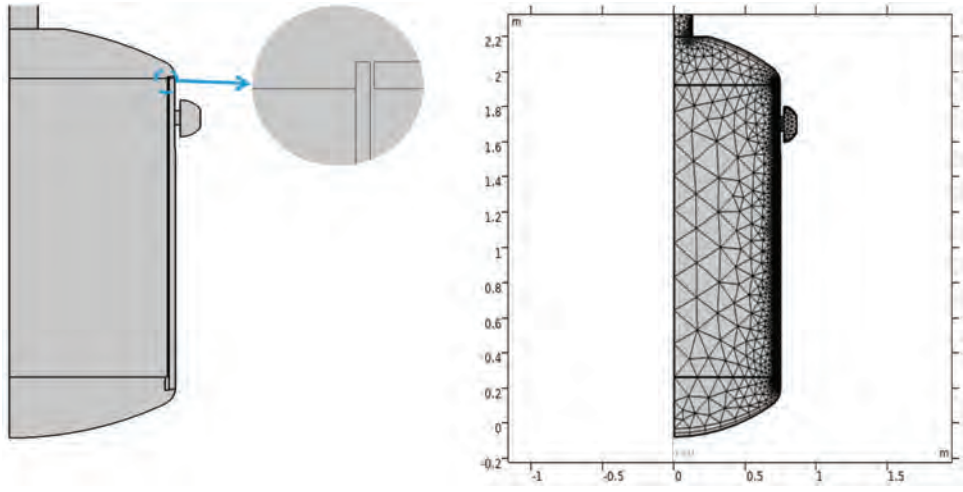

Fig. 15. (left) Geometry of the MSRE reactor vessel and (right) the mesh setting for the coupled calculations.

pump startup transient were zero velocity and eigenfunction flux distribution. The initial DNP distribution was obtained through a pseudo transient step. For the coast-down transient, the last time step solution for the startup test was used as an initial condition.

## V.B. Effect of Bypass Flow

As previously mentioned, at the nominal flow rate (1200 gpm), there was a 24-gpm bypass flow to the upper head. Additionally, there was 3 to 22 gpm passing through the annular clearances at the core can support ring. To investigate the effect of the bypass flow on the reactivity response to the flow transient, three sets of calculations were conducted using a zero, 24-gpm, and 46-gpm bypass flow. A comparison between the results for the startup test for the three cases to the experimental data is shown in Fig. 17. The bypass flow had a significant effect on the reactivity response at the initial stage of the transient where increasing the bypass flow reduced the rate of reactivity insertion. This effect could be understood by looking into the number of DNPs inside the core for each of the three cases.

Figure 18 shows how the total number of the second DNP group inside the core changed over time during the startup transient. As the bypass flow increased, the flow

TABLE VIII

Geometrical Parameters of the R-Z Model

| Component | Dimension | |
|---|---|---|
| Core | Radius (cm) | 71.33 |
| | Height (cm) | 166.19 |
| | Volume ($cm^3$) | 2.656E+6 |
| | Porosity | 0.2665 |
| Upper head | Height (cm) | 27.61 |
| | Curvature radius, cm | 147.32 |
| | Volume ($cm^3$) | 0.3134E+6 |
| | Porosity | 0.9486 |
| Lower head | Height (cm) | 34.07 |
| | Curvature radius (cm) | 147.32 |
| | Volume ($cm^3$) | 0.3931E+6 |
| | Porosity | 0.7205 |
| Distributor and downcomer | Downcomer width (cm) | 2.45 |
| | Volume ($cm^3$) | 0.3030E+6 |
| | Porosity | 0.9065 |
| Core can | Height (cm) | 174.63 |
| | Thickness (cm) | 0.642 |
| External loop | Radius (cm) | 12.85 |
| | Height (cm) | 656.66 |

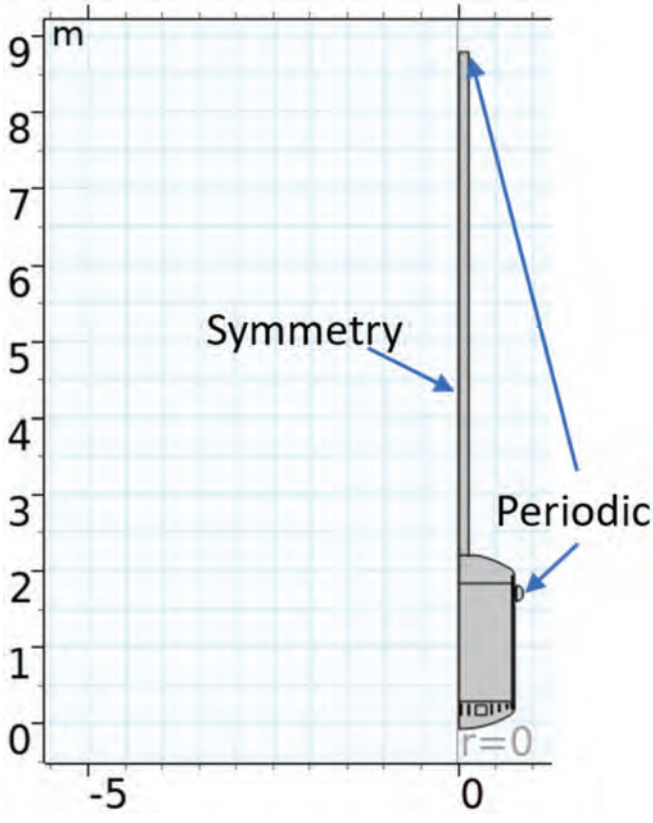


Fig. 16. Periodic boundary condition for the DNP transport model.

speed in the core was reduced, which resulted in a slower rate of DNP drift outside the core. It also reduced the minimum number of DNPs inside the core. The combined effect of these two factors reduced the rate and magnitude of reactivity insertion with increasing bypass flow.

In the three cases, the reactivity peak was significantly lower than the experimental data. Taking into consideration the expected overshooting in the inserted reactivity due to the limited speed of the control rod, a closer look into the distribution of the second DNP group $\left(t_{\frac{1}{2}} \approx 21.17\text{s}\right)$ at peak time, shown in Fig. 19, gives more insights into these results. The distribution indicated that there was a significant concentration of DNPs at the center of the core that did not drift out of the core while the recirculated salt was reentering the core at the outer region. This was caused by the nonuniform flow distribution at the core inlet at the initial phase of the transient, as depicted in Fig. 20. The figure shows a heat map of the flow speed as a function of the radial position ($y$-axis) and time ($x$-axis) during the startup test. The figure also shows that the flow speed at the outer region of the core was significantly higher than that at the center of the core during the initial phase of the transient.

This effect tended to decay out after about 30s, and the flow tended to be uniform across the core inlet. The larger flow rate at the outer region reduced the drift rate on the high DNP concentration at the core center, which in turn reduced the reactivity insertion. Following the initial stage, the reactivity response was almost independent of the bypass flow. Generally, the reactivity insertion predicted in the three cases was in excellent agreement with the experimental data. The mean absolute error in reactivity predictions compared to experimental data was 14.3 pcm, 12 pcm, and 11 pcm for no-bypass, 24-gpm, and 46-gpm cases, respectively.

The distribution of DNPs in the reactor vessel at the end of the pump startup transient ($t$ = 50s) is shown in Fig. 21. For the long-lived DNP groups, there was a considerable fraction of DNP that recirculated into the core. This caused the distribution of these groups to differ significantly from the stationary configuration. On the other hand, the distribution of the short-lived group was similar to the stationary configuration, with the peak of the concentration shifted in the direction of the fuel flow. The distribution of the sixth group ($t_{\frac{1}{2}} = 0.24\text{s}$) virtually did not differ from the stationary configuration. For the first and second groups, there was a large gradient of their concentration in the lower head due to the lack of turbulent modeling.

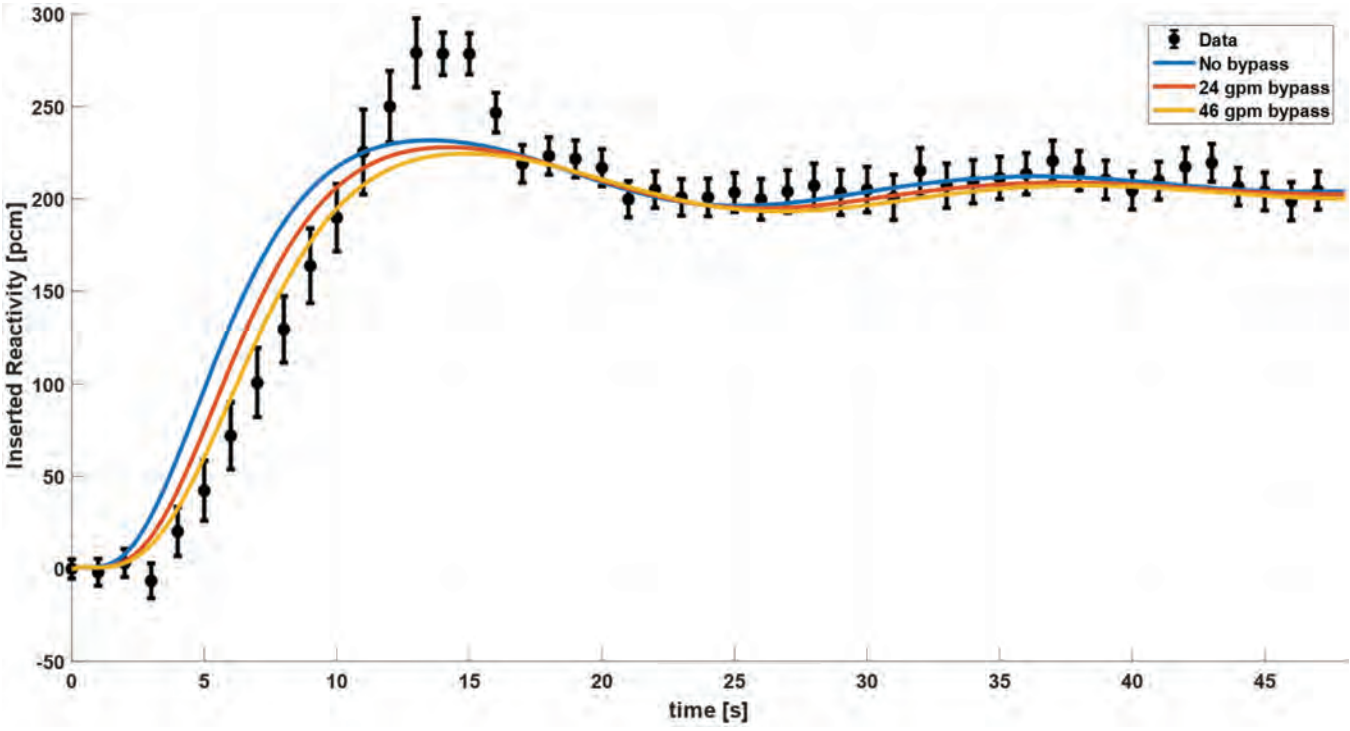


Fig. 17. Reactivity response to the startup transient using the R-Z model for the three cases of bypass flow.

The results for the coastdown transient are shown in Fig. 22. The bypass flow did not have any impact on the reactivity response. The calculated reactivity response for the coastdown transient was slightly overestimated at the end of the transient. This could be explained by investigating the velocity field during the coastdown transient.

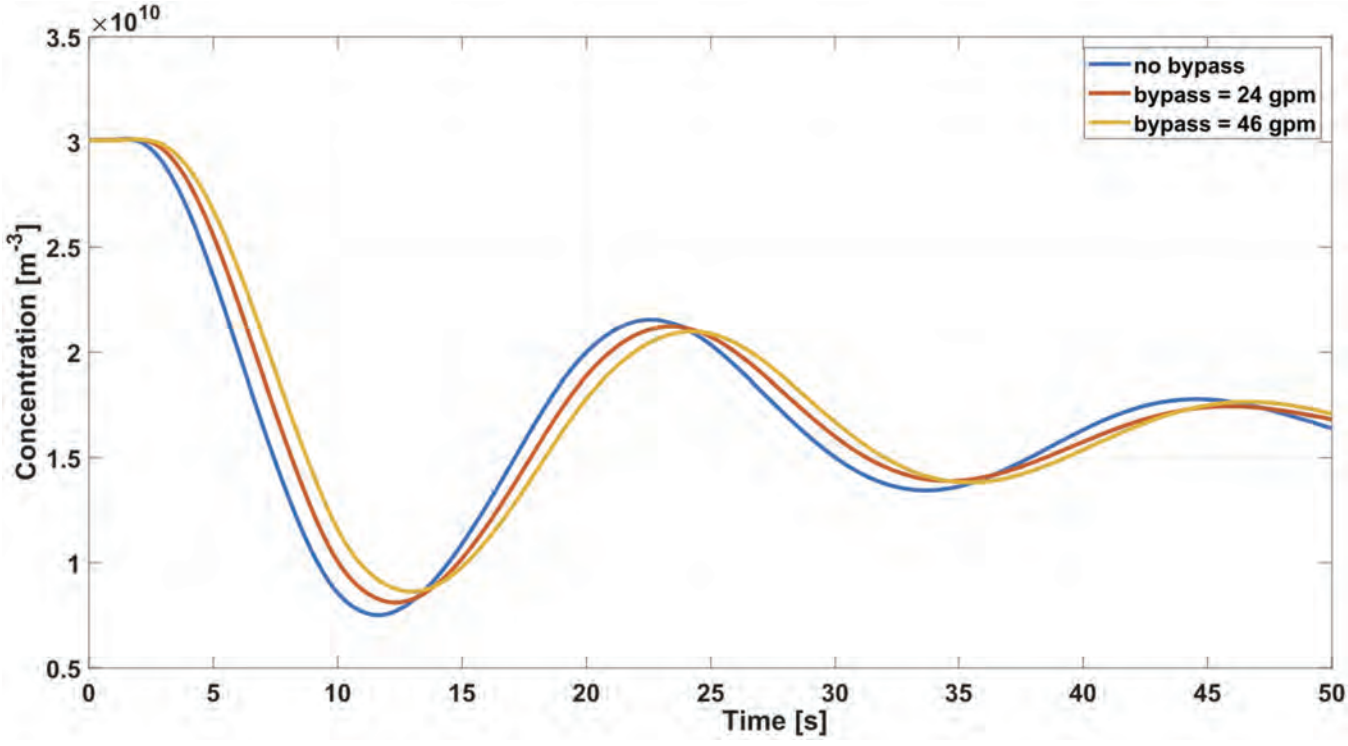


Fig. 18. Calculated number of second group of DNPs inside the core during the startup test.

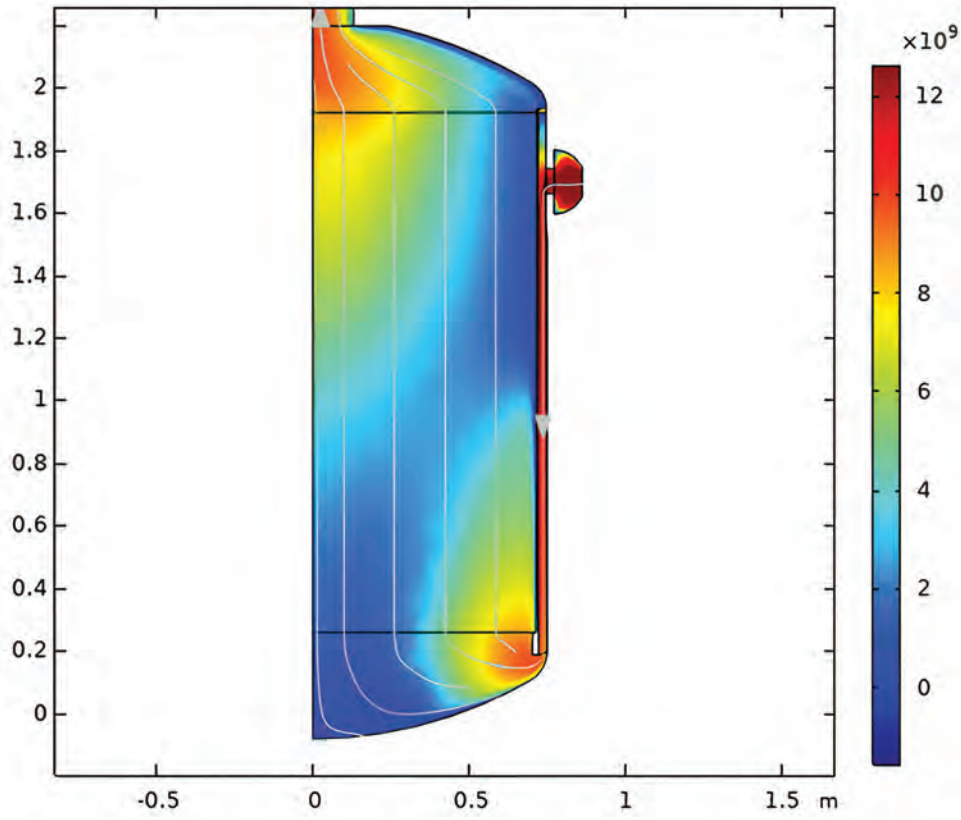


Fig. 19. Concentration of the second DNP group at $t$ = 14.2 s during the startup test for the 24-gpm bypass case.

Figure 23 shows the velocity field and the concentration of the second group of DNPs during the coastdown transient at $t$ = 40s.

As the flow rate became significantly low, flow circulation occurred in the lower head and the outer region of the core. The flow circulation at these low importance regions resulted in the loss of delayed neutrons, and hence, increased the reactivity insertion estimates. The calculated reactivity response was generally in good agreement with the experimental data. The mean absolute

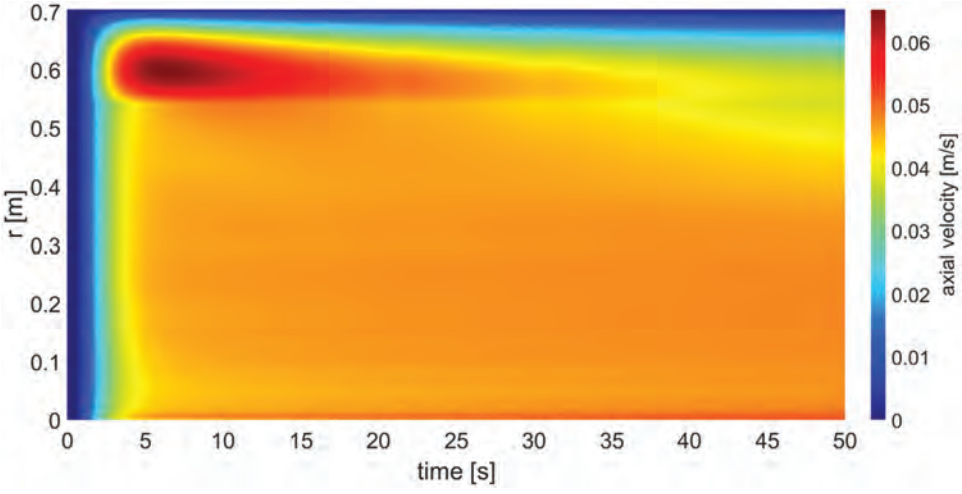


Fig. 20. Radial flow distribution at the core inlet as a function of time during the startup test.

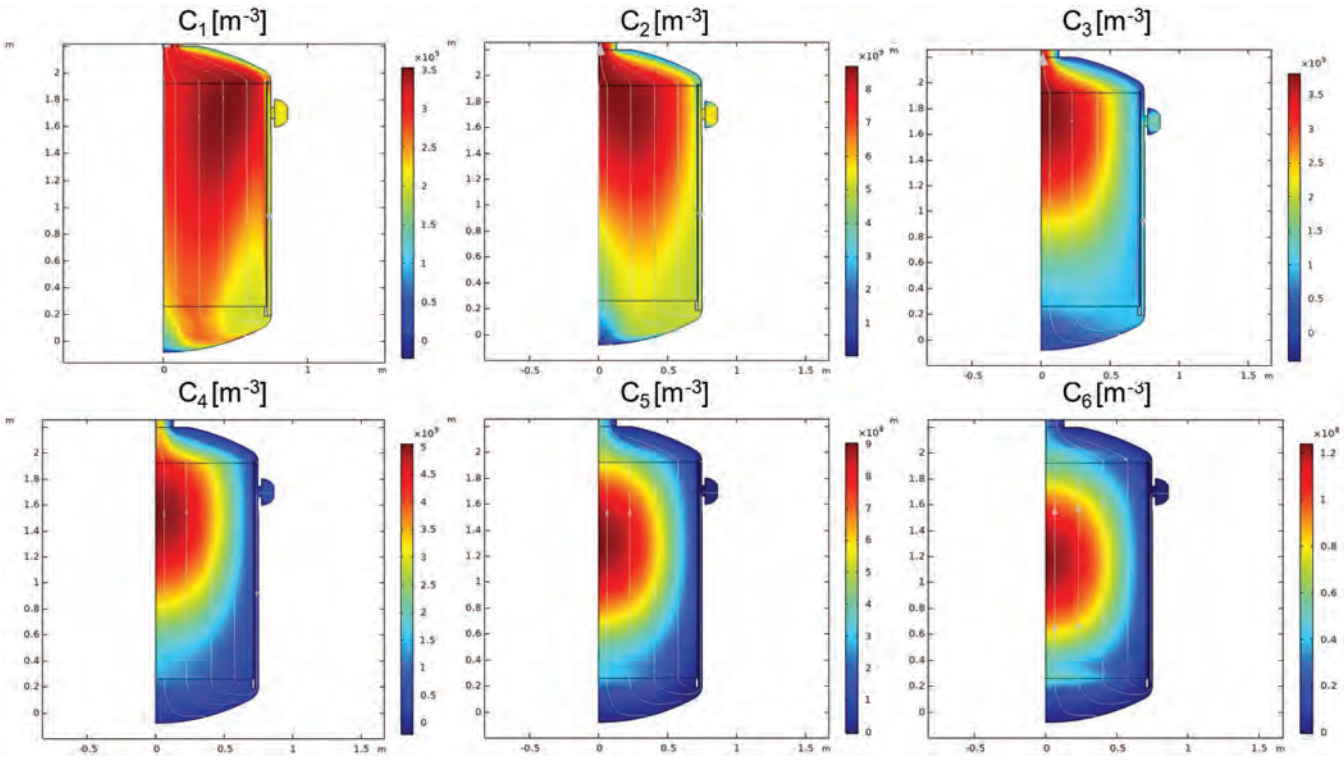


Fig. 21. DNP distribution at the end of the startup transient for the 24-gpm bypass case.

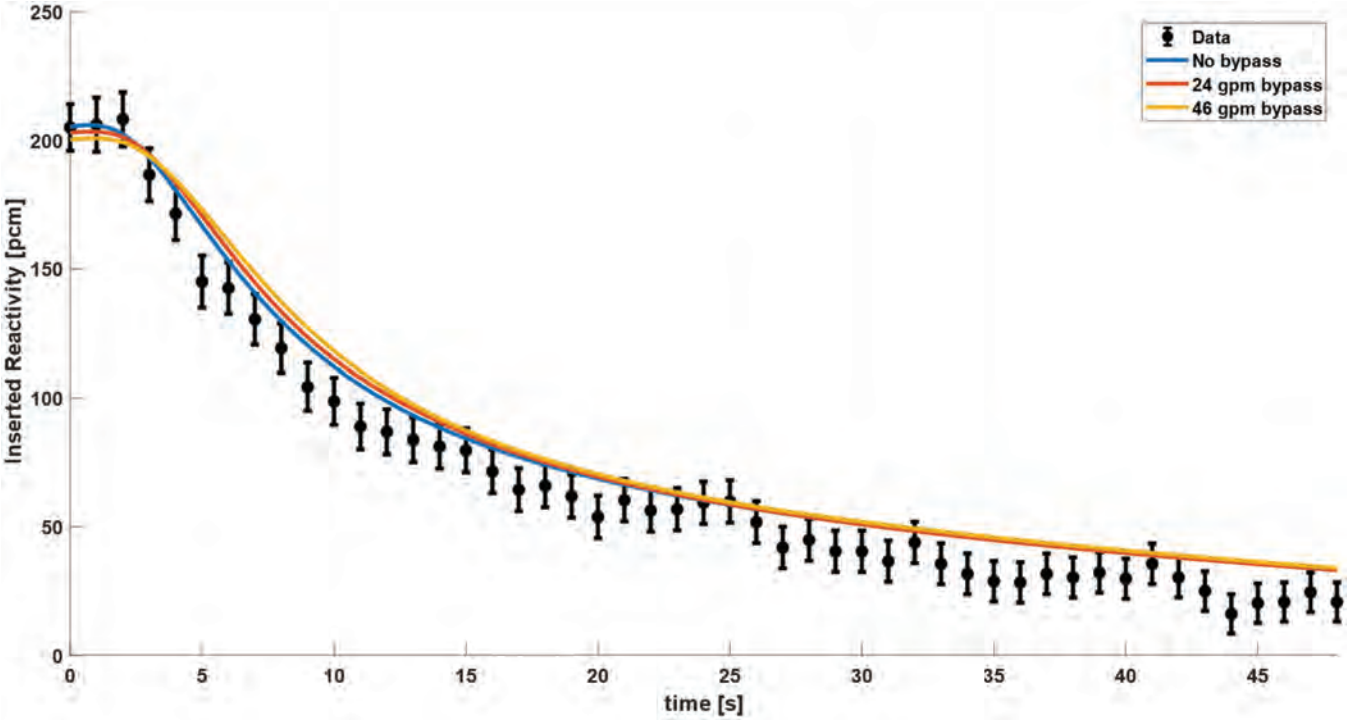


Fig. 22. Reactivity response to the coastdown transient using the R-Z model for the three cases of bypass flow.

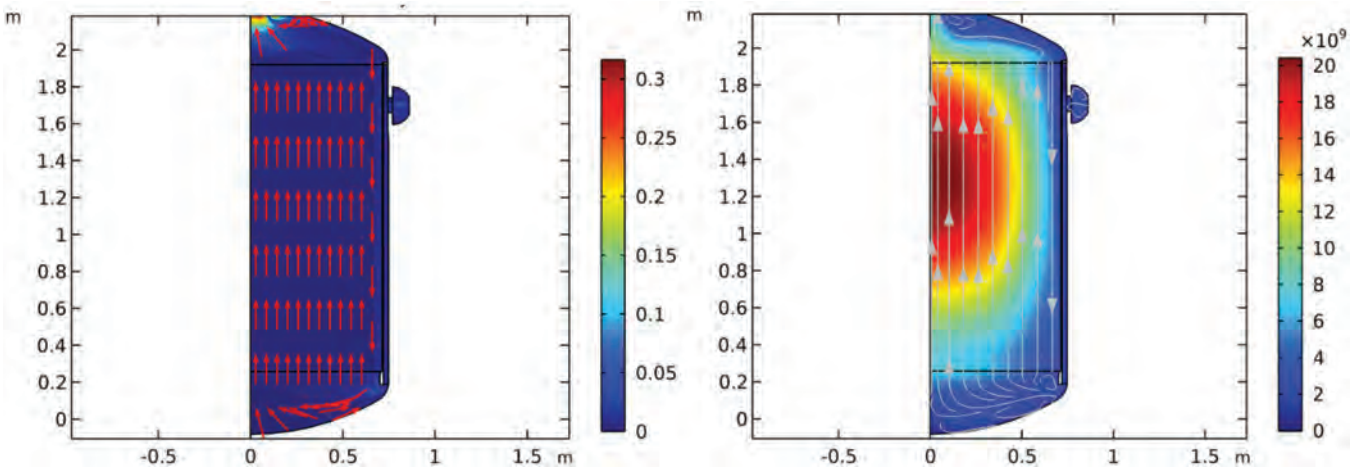


Fig. 23. (left) Velocity field and (right) concentration of the second DNP group at $t$ = 40s during the coastdown test.

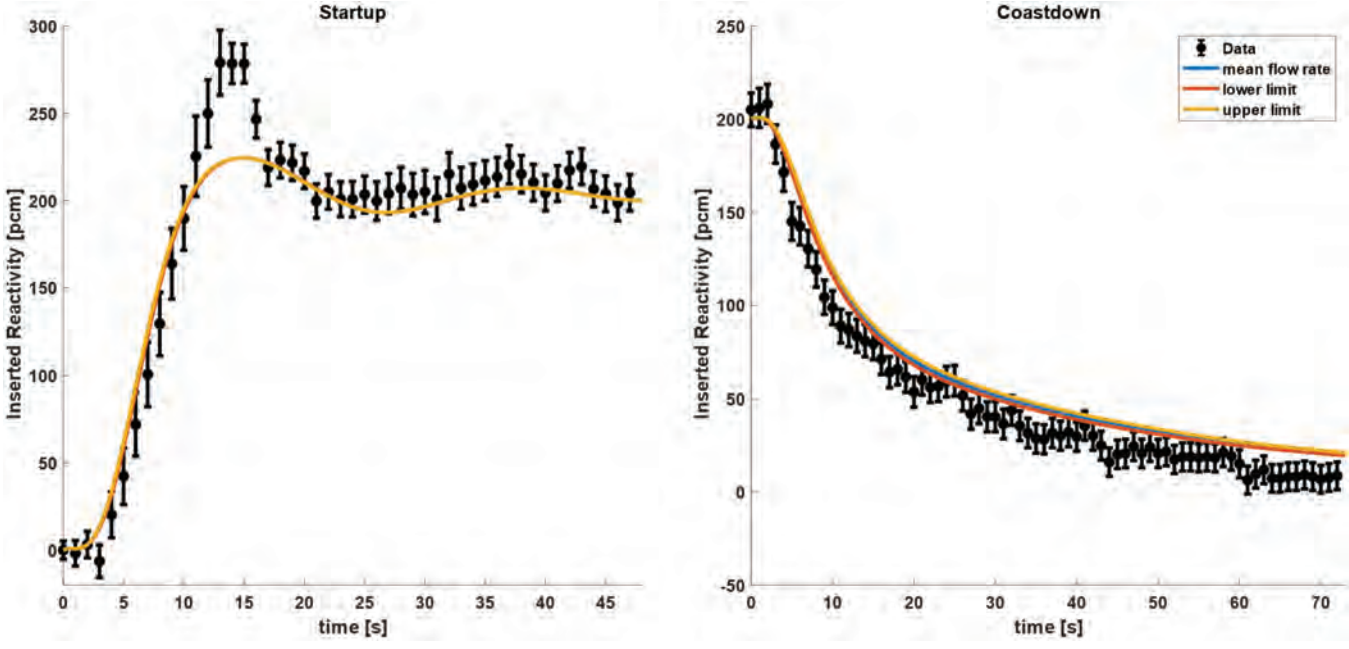


Fig. 24. Effects of the transient flow rate uncertainty on the reactivity response for the pump transient tests.

error in the reactivity response was 11 pcm, 11.5 pcm, and 12.7 pcm for no-bypass, 24-gpm, and 46-gpm cases, respectively.

## V.C. Effect of Transient Flow Uncertainty

The effect of the uncertainty in the generated transient flow rate (see Table III) was studied by comparing the reactivity response at the mean value of the generated transient flow rate to the reactivity response at the lower and upper limits [mean ± standard deviation (STD)] of the transient flow rate. The calculations were carried out assuming a 46-gpm bypass flow rate. The results are shown in Fig. 24.

The results showed that the uncertainty in the startup flow rate had a negligible effect on the reactivity response. This was due to the small uncertainty in the startup flow rate and to the rapid flow transient (~6 s) compared to the reactivity transient (~50 s). On the other hand, the reactivity response to the coastdown test showed a slight dependance on the transient flow rate.

The reactivity response changed on average by about 3 pcm between the lower and upper limits. This was due

to the slightly lager uncertainty interval for the coastdown flow rate. Also, the transient flow rate for the coastdown case had a slower rate. In general, the uncertainty in the generated flow rates, within the studied interval, had a negligible impact on the reactivity predictions.

## VI. CONCLUSIONS

In this work, a systematic study was conducted on the MSRE pump transient tests with the aim of developing a transient benchmark based on this test. The uncertainty in the experimental data was estimated using a sampling approach, taking into account the uncertainty in the rod position indicator and the integral worth curve. Two models with different fidelity levels were used to evaluate the effects of spatial resolution.

The low-order model used a 1D geometrical representation of the MSRE fuel circulation loop. The computational model solved the multigroup neutron diffusion equation, the DNP advection-diffusion equation, and the fluid flow in pipes equation. The system of equation was solved in a fully coupled scheme. The model was implemented in COMSOL, and the run time for the 1D model was about 1 min for the entire transient.

The high-order model used a R-Z 2D geometry. The structural materials inside the reactor vessel were simplified using the porous medium approximation. The 2D model solved the multigroup neutron diffusion equation, the DNP advection-diffusion equation, and the Brinkman's equation for fluid flow in porous media. The system was solved in a segregated, iterative approach. The model was implemented in COMSOL, and the run time for the 2D model was about 2 h for the entire transient.

The predictions of the 1D model showed excellent agreement with the experimental data for the coastdown transient. For the startup, the 1D model overestimated the reactivity oscillations. This was attributed to the neglection of turbulent mixing in the DNP transport model. This was resolved by using the Taylor correlation for turbulent flow in circular pipes. The model overestimated the reactivity insertion rate at the initial phase of the transient. This could be explained by the neglection of the bypass flow between the annulus and the upper plenum.

Other factors that contributed to the errors in the 1D predictions were the lack of radial distribution of flow and DNP. The 1D model was used to investigate the effect of the neutron energy discretization (i.e., group structure) on the simulation accuracy. The results showed that using the standard 2G structure with the adjoint-weighted DNFs produced the same transient response as the 8G structure with the forward-weighted DNFs. The model was also used to investigate the effect of the DNP group structures.

The high-order model calculations were conducted using a R-Z 2D geometry to reduce the computational cost of the 3D geometry. The predictions of the R-Z model for the startup test were in excellent agreement with the experimental data after the initial reactivity peak. The model significantly underestimated the reactivity peak. This was attributed to the homogenization of the lower head. As the model converged to a steady state, the flow inside the core was radially uniform, and the model predictions converged to the experimental steady state.

For the coastdown transient, the model predictions were in good agreement with the data, with the model slightly overestimating the reactivity insertion. The R-Z model was used to investigate the effect of the bypass flow on the reactivity response. The results showed that the bypass flow had a significant impact on the reactivity response at the initial phase of the startup test. Based on these results, the response of the MSRE was highly dependent on the flow features. Accurate predictions of the reactivity response would require an accurate prediction of the flow field and an accurate prediction of the DNP transport phenomena.

The benchmark models developed in this work will be submitted to the IRPhE Handbook. In the future, the methods presented in this work will be used to evaluate other MSRE transients, such as the reactivity insertion tests and the natural circulation test.

### Acknowledgments

The authors would like to express their sincere gratitude to the anonymous reviewers for their insightful comments and constructive feedback, which significantly improved the quality of this paper.

### Funding

This work was partially supported by the U.S. Department of Energy Nuclear Energy University Program project with award no. DE-NE0009162.

### Disclosure Statement

No potential conflict of interest was reported by the author(s).

## ORCID

Mohamed Elhareef http://orcid.org/0000-0001-5643-3591
Youssef Abouhussien http://orcid.org/0009-0009-6637-5909
Zeyun Wu http://orcid.org/0000-0002-6114-0352
Massimiliano Fratoni http://orcid.org/0000-0003-0452-0508
Eva Davidson http://orcid.org/0000-0001-5733-9273
Tingzhou Fei http://orcid.org/0009-0000-9504-2884
Kurt Harris http://orcid.org/0000-0002-7288-0882

## References

1. "A Technology Roadmap for Generation IV Nuclear Energy Systems: Executive Summary," U.S. Department of Energy, Nuclear Energy Research Advisory Committee, and the Generation IV International Forum (2002).
2. T. J. DOLAN, "Molten Salt Reactors and Thorium Energy," *Woodhead Publishing Series in Energy*, Woodhead Publishing, Duxford, England (2017).
3. A. SOWDER et al., "Program on Technology Innovation: Technology Assessment of a Molten Salt Reactor Design: The Liquid-Fluoride Thorium Reactor (LFTR)," 3002005460, The Electric Power Research Institute (Oct. 2015).
4. H. G. MACPHERSON, "Molten-Salt Reactor Program Quarterly Progress Report for Period Ending July 31 1960," ORNL-3014, Oak Ridge National Laboratory (1960).
5. L. LUZZI, V. D. I. MARCELLO, and A. CAMMI, *Multi-Physics Approach to the Modeling and Analysis of Molten Salt Reactors*, Nova Novinka, United Kingdom (2012).
6. "Semiannual Progress Report for Period Ending August 31 1970," ORNL-4622, Molten Salt Reactor Program, Oak Ridge National Laboratory (1970).
7. F. BOSTELMANN et al., "Modeling of the Molten Salt Reactor Experiment with SCALE," *Nucl. Technol.*, **208**, *4*, 603(2021).
8. V. SINGH et al., "Nonlinear Dynamic Model of Molten-Salt Reactor Experiment—Validation and Operational Analysis," *Ann. Nucl. Energy*, **113**, 177 (2018); https://doi.org/10.1016/j.anucene.2017.10.047.
9. M. DELPECH et al., "Benchmark of Dynamic Simulation Tools for Molten Salt Reactors," presented at the Int. Conf. GLOBAL, New Orleans, Louisiana, November 16–20, 2003.
10. M. H. ELHAREEF, T. FEI, and Z. WU, "Computational Modeling and Verification of MSR Transients via MSRE Reactivity Insertion Tests," presented at PHYSOR 2024 – Beyond the Blueprint: Pioneering Reactor Physics for Real-World Implementation, San Francisco, California, April 21–24, 2024.
11. R. C. HARVILL et al., "Steady-State and Transient Benchmarks of GOTHIC to the Molten Salt Reactor Experiment," *Nucl. Technol.*, **208**, *1*, 70 (2021); https://doi.org/10.1080/00295450.2021.1884491.
12. J. KŘEPEL et al., "DYN3D-MSR Spatial Dynamics Code for Molten Salt Reactors," *Ann. Nucl. Energy*, **34**, *6*, 449 (2007); https://doi.org/10.1016/j.anucene.2006.12.011.
13. M. K. JARADAT et al., "Development and Validation of PROTEUS-NODAL Transient Analyses Capabilities for Molten Salt Reactors," *Ann. Nucl. Energy*, **160**, 108402 (2021); https://doi.org/10.1016/j.anucene.2021.108402.
14. A. LINDSAY et al., "Introduction to Moltres: An Application for Simulation of Molten Salt Reactors," *Ann. Nucl. Energy*, **114**, 530 (2018); https://doi.org/10.1016/j.anucene.2017.12.025.
15. G. YANG et al., "Development of Coupled PROTEUS-NODAL and SAM Code System for Multiphysics Analysis of Molten Salt Reactors," *Ann. Nucl. Energy*, **168**, 108889 (2022); https://doi.org/10.1016/j.anucene.2021.108889.
16. M. K. M. JARADAT, J. ORTENSI, and G. YANG, "Multiphysics Analysis of the MSRE Experiment Using Griffin-SAM Coupled Code System," INL/CON-23-73281-Rev. 1, Idaho National Laboratory (Nov. 2023).
17. Z. WU et al., "MSRE Transient Benchmark Development and Evaluation: NEUP Project Updates," *Trans. Am. Nucl. Soc*, **127**, *1*, 1153 (2022).
18. *International Handbook of Evaluated Reactor Physics Benchmark Experiments* (*IRPhE*), Organisation for Economic Co-operation and Development/Nuclear Energy Agency (2023).
19. M. FRATONI et al., "Molten Salt Reactor Experiment Benchmark Evaluation," DOE-UCB-8542, University of California, Berkeley, California and Oak Ridge National Laboratory (May 6, 2020).
20. R. C. ROBERTSON, "MSRE Design & Operations Report Part 1: Description of Reactor Design," ORNL-TM-728, Oak Ridge National Laboratory (1965).
21. J. D. ARREGUI-MENA et al., "Microstructural Characterization of the CGB Graphite Grade from the Molten Salt Reactor Experiment," *J. Nucl. Mater.*, **582**, 154421 (2023); https://doi.org/10.1016/j.jnucmat.2023.154421.
22. R. HU et al., "SAM Theory Manual," Argonne National Laboratory (2021).
23. A. STUBSGAARD, "OPENMSR"; Github; https://github.com/openmsr/msre (current as of Dec. 27, 2023).
24. E. COMPERE et al., "Fission Product Behavior in the Molten Salt Reactor Experiment: Technical Report," ORNL-4865, Oak Ridge National Laboratory (1975).

25. B. E. PRINCE et al., "Zero-Power Physics Experiment on the Molten Salt Reactor Experiment," ORNL-4233, Oak Ridge National Laboratory (1968).

26. R. B. BRIGGS, "Molten-Salt Reactor Program Semi-Annual Progress Report," ORNL-3872, Oak Ridge National Laboratory (1965).

27. J. R. TALLACKSON, "MSRE Design and Operations Report, Part II.A: Nuclear and Process Instrumentation," ORNL-TM-0729A, Oak Ridge National Laboratory (1968).

28. R. H. GUYMON et al., "MSRE Design and Operations Report, Part XI: Test Program," ORNL-TM-0911, Oak Ridge National Laboratory (1966).

29. M. ELHAREEF and Z. WU, "A New Approach to Predict Pump Transient Phenomena in Molten Salt Reactor Experiment (MSRE) by Missing Data Identification and Regeneration," *Nucl. Eng. Des.*, **424**, 113292 (2024); https://doi.org/10.1016/j.nucengdes.2024.113292.

30. M. H. ELHAREEF and Z. WU, "Uncertainty Analysis on the Pump Flow Transient Phenomena in the Molten Salt Reactor Experiment," *Trans. Am. Nucl. Soc*, **130**, *1*, 450 (2024).

31. J. LI, X. LIN, and Z. CHEN, *Finite Volume Methods for the Incompressible Navier-Stokes Equations*, Vol. 2022, pp. 53–82, Springer, London (2022).

32. M. WANG et al., "Recent Progress of CFD Applications in PWR Thermal Hydraulics Study and Future Directions," *Ann. Nucl. Energy*, **150**, 107836 (2021); https://doi.org/10.1016/j.anucene.2020.107836.

33. D. BESTION, "System Code Models and Capabilities," presented at Thicket-2008, Italy, May 5–9, 2008.

34. I. CLIFFORD, K. IVANOV, and M. AVRAMOVA, "A General Coarse and Fine Mesh Solution Scheme for Fluid Flow Modeling in VTRS," presented at the Int. Conf. on Mathematics and Computational Methods Applied to Nuclear Science and Engineering (M&C 2011), Rio de Janeiro, RJ, Brazil, May 8–12, 2011.

35. H. ZHANG et al., *RELAP-7 User's Guide*, INL/EXT-14-33977, Idaho National Laboratory (Mar. 2018).

36. A. NOVAK et al., "Pronghorn: A Multidimensional Coarse-Mesh Application for Advanced Reactor Thermal Hydraulics," *Nucl. Technol.*, **207**, *7*, 1015 (2021); https://doi.org/10.1080/00295450.2020.1825307.

37. C. FIORINA et al., "GeN-Foam: A Novel OpenFOAM® Based Multi-Physics Solver for 2D/3D Transient Analysis of Nuclear Reactors," *Nucl. Eng. Des.*, **294**, 24 (2015); https://doi.org/10.1016/j.nucengdes.2015.05.035.

38. M. ELHAREEF, Z. WU, and M. FRATONI, "A Consistent One-Dimensional Multigroup Diffusion Model for Molten Salt Reactor Neutronics Calculations," *J. Nucl. Eng.*, **4**, 654 (2023); https://doi.org/10.3390/jne4040041.

39. *Pipe Flow Module User's Guide*, pp. 47–59, COMSOL Multiphysics®, COMSOL AB, Stockholm, Sweden (2023); www.comsol.com (current as of Feb. 24, 2025).

40. D. NIELD and A. BEJAN, *Convection in Porous Media*, 5th Ed., Springer (2017).

41. M. HONARPOUR and S. M. MAHMOOD, "Relative-Permeability Measurements: An Overview," *J. Petrol. Tech.*, **40**, *8*, 963 (1988); https://doi.org/10.2118/18565-PA.

42. S. DULLA, E. H. MUND, and P. RAVETTO, "The Quasi-Static Method Revisited," *Prog. Nucl. Energy*, **50**, *8*, 908 (2008); https://doi.org/10.1016/j.pnucene.2008.04.009.

43. X. ZHOU et al., "Development of a Neutron Space-Time Kinetics Solver with Improved Quasi-Static Method Based on OpenFOAM," *Nucl. Eng. Des.*, **419**, 112990 (2024); https://doi.org/10.1016/j.nucengdes.2024.112990.

44. M. S. CHENG and Z. M. DAI, "Development of a Three-Dimension Multi-Physics Code for Molten Salt Fast Reactor," *Nucl. Sci. Tech.*, **25**, 010601 (2014).

45. D. WOOTEN and J. J. POWERS, "A Review of Molten Salt Reactor Kinetics Models," *Nucl. Sci. Eng.*, **191**, *3*, 203 (2018); https://doi.org/10.1080/00295639.2018.1480182.

46. M. AUFIERO et al., "Calculating the Effective Delayed Neutron Fraction in the Molten Salt Fast Reactor: Analytical, Deterministic and Monte Carlo Approaches," *Ann. Nucl. Energy*, **65**, 78 (2014); https://doi.org/10.1016/j.anucene.2013.10.015.

47. "COMSOL Multiphysics®," COMSOL AB, Stockholm, Sweden; www.comsol.com (current as of Feb. 24, 2025).

48. D. SHEN et al., "Reactor Physics Benchmark of the First Criticality in the Molten Salt Reactor Experiment," *Nucl. Sci. Eng.*, **195**, *8*, 825 (2021); https://doi.org/10.1080/00295639.2021.1880850.

49. D. A. BROWN et al., "ENDF/B-VIII.0: The 8th Major Release of the Nuclear Reaction Data Library with CIELO-Project Cross Sections, New Standards and Thermal Scattering Data," *Nucl. Data Sheets*, **148**, 1 (2018).

50. M. ZANETTI et al., "An innovative approach to dynamics modeling and simulations of the Molten Salt Reactor Experiment," *Proc. Int. Conference PHYSOR 2014*, Kyoto, Japan (2014).

51. M. H. ELHAREEF and Z. WU, "Effect of Turbulent Diffusion on Delayed Neutron Precursors in the Molten Salt Reactor Experiment (MSRE)," presented at the ANS Winter Mtg., Orlando Florida, November 17–21, 2024.

52. G. TAYLOR, "The Dispersion of Matter in Turbulent Flow Through a Pipe," *Proc. Royal Society of London, Series A*, **223**, 1155, 446 (1954).

53. A. J. M. PLOMPEN et al., "The Joint Evaluated Fission and Fusion Nuclear Data Library, JEFF-3.3," *Eur. Phys. J. A.*, **56**, 181 (July 2020).